



Available online at www.sciencedirect.com

ScienceDirect

Comput. Methods Appl. Mech. Engrg. 404 (2023) 115745

**Computer methods
in applied
mechanics and
engineering**

www.elsevier.com/locate/cma

Explicit layout optimization of complex rib-reinforced thin-walled structures via computational conformal mapping (CCM)

Xudong Jiang^a, Wendong Huo^{a,*}, Chang Liu^{a,b,*}, Zongliang Du^{a,b}, Xiaoyu Zhang^c,
Xiao Li^c, Xu Guo^{a,b,*}

^a State Key Laboratory of Structural Analysis for Industrial Equipment, Department of Engineering Mechanics, Dalian University of Technology, Dalian, 116023, PR China

^b Ningbo Institute of Dalian University of Technology, Ningbo, 315016, PR China

^c Beijing Institute of Spacecraft System Engineering, Beijing 100094, PR China

Received 22 July 2022; received in revised form 4 October 2022; accepted 27 October 2022

Available online 21 November 2022

Abstract

Rib-reinforced thin-walled structures are commonly used in various important industrial fields. In this paper, an explicit layout optimization method is developed to design rib-reinforced thin-walled structures with complex geometries. The proposed method includes the following two key steps: (1) parameterizing the complex surfaces with the use of the Computational Conformal Mapping (CCM) technique, and (2) carrying out explicit layout optimization under the Moving Morphable Component (MMC)-based solution framework integrating with the surface cutting operation and the multi-patch stitching scheme on the parametric space. In addition, both the base panel and the reinforced ribs are modeled by 3D shell elements, which have the advantage of providing accurate mechanical analysis results for thin-walled structures with less computational effort. The proposed method can provide clear rib-reinforced layouts of thin-walled structures with complex geometries and the optimized results can be directly imported into CAD/CAE systems without any post-processing. Several representative numerical examples, including a rib-reinforced blunt shell, a rib-reinforced torus-shaped shell, a rib-reinforced flower-shaped shell and a rib-reinforced tee-branch pipe, are presented to validate the effectiveness of the proposed method.

© 2022 Elsevier B.V. All rights reserved.

Keywords: Rib-reinforced thin-walled structures; Complex surfaces; Moving Morphable Component (MMC); Computational Conformal Mapping (CCM); Surface parameterization

1. Introduction

Thin-walled structure, as a lightweight and easy-to-manufactured structural form, is widely used as the main force-carrying component in much high-end industrial equipment, such as submarines, rockets, and spacecraft [1–4]. However, thin-walled structures are usually serviced in complex loading conditions and are often susceptible to large deformation, strength failure, buckling failure, etc. To enhance the rigidity, strength, stability and dynamic

* Corresponding authors at: State Key Laboratory of Structural Analysis for Industrial Equipment, Department of Engineering Mechanics, Dalian University of Technology, Dalian, 116023, PR China.

E-mail addresses: huowd@mail.dlut.edu.cn (W. Huo), c.liu@dlut.edu.cn (C. Liu), guoxu@dlut.edu.cn (X. Guo).

performance of such structures, rib-reinforcement is commonly used for the design of thin-walled structures. Since the size, shape and layout of the ribs can greatly affect the performance of the structure, design optimization of rib-reinforced thin-walled structures is very demanding in practical engineering applications and has attracted great interest among researchers.

The earliest research on layout/topology optimization of rib-reinforced thin-walled structures can be traced back to the pioneering works by Cheng and Olhoff [5,6]. Since then, many related works have been carried out and a lot of powerful methods have been proposed. On the one hand, many attempts have been made under the pixel-based optimization framework using multi-layer solid elements for finite element analysis and rib-layout characterization simultaneously. For example, Ansola et al. [7] combined the ribbed microstructure and the homogenization technique for shape and reinforcement layout optimization of shell structures. Liu et al. [8] developed a so-called H-DGTP method under the density-based optimization framework and successfully obtained the optimal layout and size of stiffeners of thin-walled structures with casting constraints satisfied. In the work of Dugré et al. [9], the design space of stiffened panels can be modeled by the three-dimensional solid elements or the two-dimensional Mindlin shell elements, and the density variables of elements are modified to obtain different stiffener layouts. Saleem et al. [10] presented a novel approach to optimizing the ribbed-stiffened machined structures based on the SIMP method and the evolutionary genetic algorithm. To design large-scale rib-reinforced thin-walled structures, Aage et al. [11] implemented a high-performance computational tool on a supercomputer and applied it to the design of the ribbed aircraft wing structure with a giga-voxel resolution based on the SIMP method. On the other hand, smeared-out models based on various structural elements (such as beam element, plate element and shell element) are also integrated with different optimization techniques for the optimal design of rib-reinforced thin-walled structures. Lagaros et al. [12] invented an efficient and robust optimization algorithm for the design of reinforced shell structures. In that method, shell elements and beam elements are adopted to simulate the base panel and the rib reinforcement, respectively, and the flange of the beam cross-section is supposed to be rigidly connected to the base panel. Hao et al. [13,14] proposed a hybrid optimization method based on a smeared stiffener method to optimize the size and layout of ribs of thin-walled cylindrical shells. Later on, Wang et al. [15] improved the traditional smeared stiffener method and proposed an effective numerical-based smear-stiffener method to further improve the efficiency of analysis and optimization of stiffened shell structures. For layout optimization of grid-stiffened thin-walled structures with sparse stiffeners, Wang et al. [16,17] used an equivalent model with ribs embedded in the laminate skin to improve the deformation compatibility between the skin and the stiffener. In addition to the aforementioned works, many novel optimization methods constructed on the basis of bionic growth simulation and smeared-out/equivalent models have also emerged over the last decades and have been successfully applied to enhance the various mechanical performances of rib-reinforced thin-walled structures [18–23]. Some other recent interesting works about the optimization of rib-reinforced thin-walled structures can be referred to [24–30].

In recent years, researchers have increasingly focused on the optimization of thin-walled structures with complex curved surfaces. For example, Träff et al. [31] combined multigrid-based high-performance computing technique and density method to solve topology optimization problems for ultra-large-scale thin-walled structures. Deng et al. [32] pointed out that when applying the density method to topology optimization problems on surfaces, the filter formulation should be modified according to the geometry of surfaces, which is essential for alleviating numerical instabilities (e.g. checkboard phenomenon, islanding effect and grey elements) effectively. Hassani et al. [33] developed an integrated approach for simultaneous shape and topology optimization of thin-walled structures where NURBS surfaces are used to model and control the shape of the structural geometry. To solve stress-constrained topology optimization problems of shell structures, Zhang et al. [34] developed an IGA/TSA-based Moving Morphable Void approach, in which the geometry of shells is described using NURBS surfaces rather than discrete elements. As the industry standard and basic language of geometry's representation in computer-aided design (CAD) systems [35], spline-type descriptions can establish a geometric mapping between parametric domain and complex surfaces with smooth analytical functions. Besides spline-type surfaces, the mesh parameterization technique, which aims at establishing a bijective mapping from the 3D mesh model of a given surface to a planar parametric domain at the level of discrete elements and nodes, also has the potential of optimizing the topology of complex thin-walled structures. Zhang et al. [36] proposed a combined parameterization approach for stiffener layout optimization of complex surfaces. In their work, the mesh parameterization technique based on the energy minimization method and cutting method is utilized to build the mapping relationship between the 3D surface mesh and the corresponding planar parametric domain, while the B-spline parameterization is applied to describe the

material distribution of the stiffener layout. Ye et al. [37] first introduced the conformal parameterization technique to the field of topology optimization and developed a level set-based method for optimizing the topologies of thin-walled structures. With the use of the computational conformal mapping technique, Huo et al. [38] realized topology optimization of shell structures under the framework of the Moving Morphable Components (MMC) method. In that work, surface cutting operation is utilized to enhance the robustness of algorithms and a multi-patch stitching scheme is integrated to alleviate the distortion of single-patch parameterization, which greatly reduces the nonlinearity of optimization problems caused by the mapping process. Different from ordinary homeomorphisms, the angle-preserving property of conformal mapping ensures the mesh quality of the planar parametric domain, which is essential for the fidelity of geometry modeling (level set function/components).

It should be pointed out that although the aforementioned works have indeed provided some effective strategies for the optimization of the rib-reinforced thin-walled structures, there are still some challenging problems that deserve to be further addressed. For example, in some of the optimized results from the density-based methods, only vague material distributions rather than distinct reinforced-rib layouts are obtained, one must resort to a laborious post-processing process to identify the main structural features (e.g., ribs) in the optimized results for subsequent design and manufacturing treatment. Besides, a relatively dense mesh is usually required along the thickness direction of the thin-walled structure when 3D solid elements are used for structural analysis, which inevitably leads to a huge amount of computation. On the other hand, when smeared-out models combined with various types of elements are utilized to calculate the structural responses, it is usually challenging to predict local structural behaviors (i.e., local stress and local buckling mode) with enough accuracy. Most significantly, most of the existing methods can only address the reinforced-rib layout optimization problems where the geometries of the involved thin-walled structures are parameterized by a single patch, and cannot be extended to the multi-patch cases, which are undoubtedly more useful and challenging.

In view of the above problems, the purpose of the present work is to develop an explicit layout optimization method under the MMC-based solution framework for optimizing the layout of rib-reinforced thin-walled structures with complex geometries. By introducing the computational conformal mapping (CCM) technique, the complex surface of a thin-walled structure is parameterized first, and then the MMC-based solution framework is utilized to construct the rib-reinforced model in the parametric space and map it into the physical space for the subsequent optimization procedure. Actually, in the present work, by leveraging the surface cutting operation and multi-patch stitching scheme, the proposed method has the capability of handling rib layout optimization problems on thin-walled structures with arbitrary complex geometries. Furthermore, in the proposed method, the considered thin-walled structure is discretized and analyzed by shell elements, which greatly reduces the computational effort compared with traditional treatment where 3D solid elements are used. Also thanks to the natural merit of the explicit optimization framework, clear optimized rib-reinforced patterns and explicit optimized size parameters of the ribs (e.g., height, width and thickness) can be obtained without any post-processing, which is urgently needed in practical engineering applications.

The rest of this paper is organized as follows. In Section 2, the theoretical foundations of the proposed method, including the MMC method, the CCM technique and the geometry description of thin-walled components on complex surfaces, are provided. The corresponding problem formulation is presented in Section 3 and the numerical implementation procedures are described in detail in Section 4. Several representative numerical examples are investigated in Section 5 to examine the numerical performance of the proposed method. Finally, some concluding remarks are given in the last section of the paper.

2. Theoretical foundations

2.1. Moving Morphable Component (MMC) method under the Lagrangian description-based framework

As an explicit topology optimization method, the MMC method was firstly proposed by Guo et al. [39] for the purpose of doing topology optimization explicitly and geometrically. Different from the conventional topology optimization methods, where the structures are constructed by a set of density-based pixel elements, a group of components described by explicit geometric parameters are regarded as the basic design members for structural optimization in the MMC method. Through the moving, deforming, merging and overlapping of these components, the optimized structural topology/layout can finally be obtained (see Fig. 1 for reference).

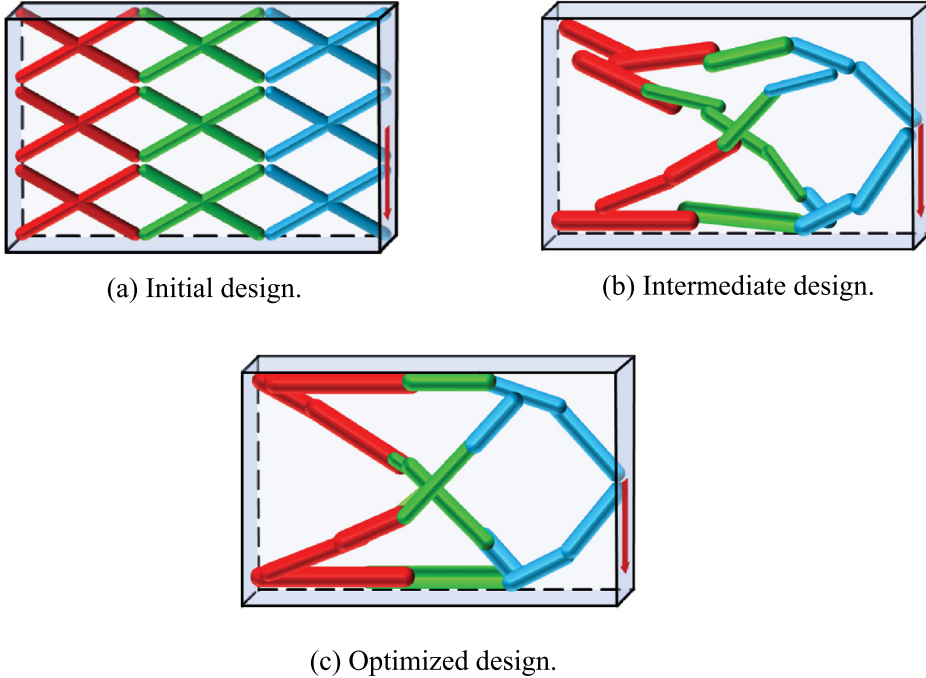


Fig. 1. An illustration of the basic idea of the MMC method.

Actually, in the MMC method, both Eulerian and Lagrangian descriptions can be utilized to build the geometry, analysis and optimization models [40]. Considering the fact that the Lagrangian description is more pertinent to achieving a fully explicit geometry description of rib-reinforced thin-walled structures and constructing more effective structural analysis models based on body-fitted FE mesh, in the present work, both the problem formulation and corresponding optimization-solution procedures are established based on a pure Lagrangian description.

Under the Lagrangian description, for a typical cuboid component as shown in Fig. 2(a), the profile of its outer boundaries can be explicitly represented as follows:

$$\mathbf{S}_1(\mu, \eta) = \mathbf{S}_0(\mu, \eta) + \frac{t}{2} \mathbf{n}_1, \quad (2.1a)$$

$$\mathbf{S}_2(\mu, \eta) = \mathbf{S}_0(\mu, \eta) - \frac{t}{2} \mathbf{n}_1, \quad (2.1b)$$

$$\mathbf{S}_3(\eta, r) = \mathbf{S}_0(0, \eta) + \frac{(1-2r)t}{2} \mathbf{n}_1, \quad (2.1c)$$

$$\mathbf{S}_4(\eta, r) = \mathbf{S}_0(1, \eta) + \frac{(1-2r)t}{2} \mathbf{n}_1, \quad (2.1d)$$

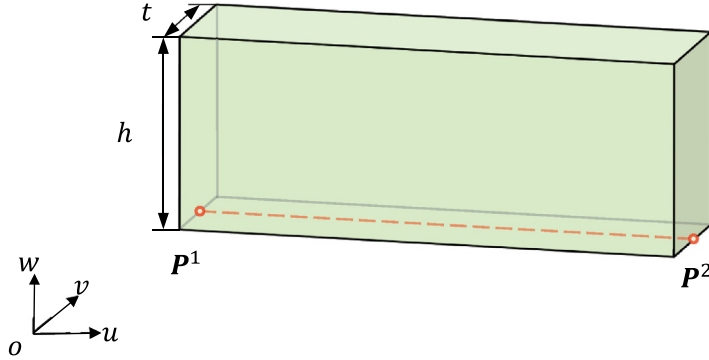
$$\mathbf{S}_5(\mu, r) = \mathbf{S}_0(\mu, 0) + \frac{(1-2r)t}{2} \mathbf{n}_1, \quad (2.1e)$$

$$\mathbf{S}_6(\mu, r) = \mathbf{S}_0(\mu, 1) + \frac{(1-2r)t}{2} \mathbf{n}_1, \quad (2.1f)$$

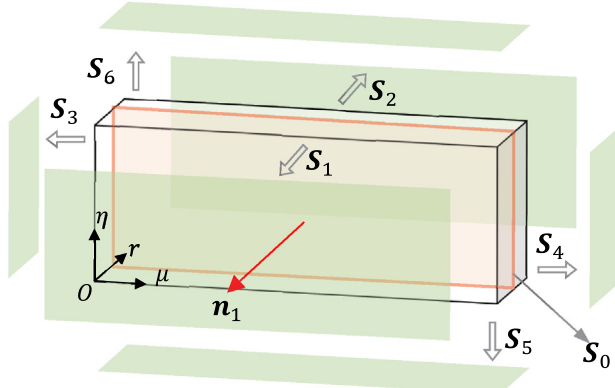
where $\mathbf{S}_0(\mu, \eta)$ represents the mid-surface of the component and it can be written as

$$\mathbf{S}_0(\mu, \eta) = (1-\mu) \mathbf{P}^1 + \mu \mathbf{P}^2 + \eta \begin{pmatrix} 0 \\ 0 \\ h \end{pmatrix}. \quad (2.2)$$

In Eqs. (2.1) and (2.2), t and h represent the thickness and height of the cuboid component, respectively. $\mathbf{P}^1 = (p_u^1, p_v^1, 0)^\top$ and $\mathbf{P}^2 = (p_u^2, p_v^2, 0)^\top$ are the coordinates of the two endpoints of the component's skeleton $\overline{\mathbf{P}^1 \mathbf{P}^2}$.



(a) Geometry model.



(b) Outer boundaries.

Fig. 2. Geometry description of a 3D cuboid component.

The symbol n_1 denotes the outer normal vector of the outer boundary S_1 . In addition, the symbols μ , η and r with $\mu \in [0, 1]$, $\eta \in [0, 1]$ and $r \in [0, 1]$ are the introduced local coordinates along the length, height and thickness direction of the component (see Fig. 2(b) for reference).

2.2. Computational conformal mapping (CCM)

The MMC method possesses the advantages of explicit geometric parameters, fewer amount of design variables and easy linking with the CAD system, and has been successfully used in the optimization of many engineering structures. However, most of these works based on MMC methods are to carry out topology optimization for structures in a regular 2D/3D design domain. For layout optimization of complex rib-reinforced thin-walled structures, since the component-based ribs must be guaranteed to always attach to the complex surface during the optimization process, it is difficult to directly apply the current MMC method.

To achieve an explicit geometry description of the component-based ribs on the complex surface and to ensure the fit of the ribs to the base surface, the middle surface of the complex thin-walled structure must first be parameterized, which is usually a challenging problem. Fortunately, with the development of computer graphics, such powerful tools

as quasi-conformal/conformal mapping techniques have been invented and effectively used in various fascinating applications [41–44]. In the present work, the computational conformal mapping technique developed in [45,46] is employed to minimize the angular distortion, which makes the parameterization useful and applicable. Instead of obtaining the conformal mapping directly, the current algorithm constructs a mapping composed of two quasi-conformal mappings with proper Beltrami coefficients to achieve conformality and bijectivity, which reduces the difficulty of problem solution significantly. The first is a disk harmonic map, which can be easily obtained by solving a system of elliptic partial differential equations. More explicitly, let \mathcal{S} be a simply-connected open surface, and \mathbb{D} be the target planar unit disk in the complex plane \mathbb{C} (see Fig. 3(a)). The harmonic mapping $f_1: \mathcal{S} \rightarrow \mathbb{D} \subset \mathbb{C}$ to be constructed satisfies the following equations

$$\begin{cases} \Delta_{\mathcal{S}} f_1 = 0, \text{ on } \mathcal{S}, \\ f_1(\partial \mathcal{S}) = \partial \mathbb{D} \end{cases} \quad (2.3)$$

where $\Delta_{\mathcal{S}}$ represents the Laplace–Beltrami operator defined on surface \mathcal{S} and Eq. (2.3) is solved by the finite element method [47]. Note that the harmonic mapping $f_1: \mathcal{S} \rightarrow \mathbb{D}$ is constructed to realize the required surface parameterization, which is in general not conformal. Hence, another quasi-conformal mapping f_2 is also constructed to alleviate the angular distortions by resorting to the scheme developed in [45]. Suppose that $f_2(z = x + iy) = u(x, y) + iv(x, y): \mathbb{D} \rightarrow \mathcal{M}$ is a quasi-conformal mapping from \mathbb{D} to a planar parameter domain \mathcal{M} (see Fig. 3(b)) (here (x, y) and (u, v) are the corresponding coordinates on the unit disk \mathbb{D} and the parameter domain \mathcal{M}) and denote the Beltrami coefficient of the inverse mapping of f_1 by $\mu_{f_1^{-1}} = \rho + i\tau$ (here ρ and τ are the real and imaginary part of $\mu_{f_1^{-1}}$ respectively), then $f_2 = u + iv$ can be found by solving the following generalized Laplace equations [45] using finite element method:

$$\begin{cases} \nabla \cdot (\mathbf{A}(\nabla u)) = 0, \\ \nabla \cdot (\mathbf{A}(\nabla v)) = 0, \end{cases} \quad (2.4)$$

where $\nabla(\cdot) = \left(\frac{\partial(\cdot)}{\partial x}, \frac{\partial(\cdot)}{\partial y} \right)^T$, $\mathbf{A} = \begin{pmatrix} \alpha_1 & \alpha_2 \\ \alpha_2 & \alpha_3 \end{pmatrix}$ and $\alpha_1 = \frac{(\rho-1)^2+\tau^2}{1-\rho^2-\tau^2}$, $\alpha_2 = -\frac{2\tau}{1-\rho^2-\tau^2}$, $\alpha_3 = \frac{(\rho+1)^2+\tau^2}{1-\rho^2-\tau^2}$. Once the two quasi-conformal mappings f_1 and f_2 are determined, the required conformal mapping $f: \mathcal{S} \rightarrow \mathcal{M}$ can be established as $f = f_2 \circ f_1$. The angular-preserving property of the constructed mapping ensures the high quality of meshes in the parametric space, which further reduces the distortion of reinforced-ribs on thin-walled structures caused by the parameterization process. Compared with existing methods, the optimization results obtained by the proposed method can be imported to CAD systems without complex post-processing owing to the parameterized description of the geometry/layout of reinforcement ribs. On the other hand, the proposed method needs some extra preprocessing process to construct the conformal mappings. However, these mappings are only required to be constructed once before the optimization process and are therefore totally decoupled from the design iteration.

2.3. Geometry description of reinforced-ribs on complex surfaces

As shown in Fig. 4, a typical rib-reinforced thin-walled structure can be viewed as being assembled of a base panel and several reinforced thin-walled components. It is worth noting that the bottom of each component must perfectly adhere to the curved surface of the base panel. As mentioned in Section 2.2, since the shape of the curved surface is commonly irregular and complex, it is difficult to directly construct these curved-shape thin-walled components on the base panel and describe the geometry of each component. To overcome this problem, the parameterization from \mathcal{S} to \mathcal{M} established by the conformal mapping is employed to implement the transformation of components in the parametric space to components in the physical space. To be specific, the components are first laid out in parameter space and described explicitly via Eqs. (2.1) and (2.2), then mapped to the physical space based on conformal mapping (see Fig. 5 for reference). In the following, we elaborate on the geometric description and generation process of components in the physical space.

Taking the component in Fig. 5 as an example, since the thickness of the thin-walled component is usually much smaller than the characteristic length scales of its other two dimensions, only the mid-surface S_0 of the component is first modeled in the parametric space as shown in Fig. 6(a). The corresponding mid-surface S'_0 of the component in the physical space obtained by the mapping is shown in Fig. 6(b), where the point $P' = (x, y, z)^T$ on S'_0 and

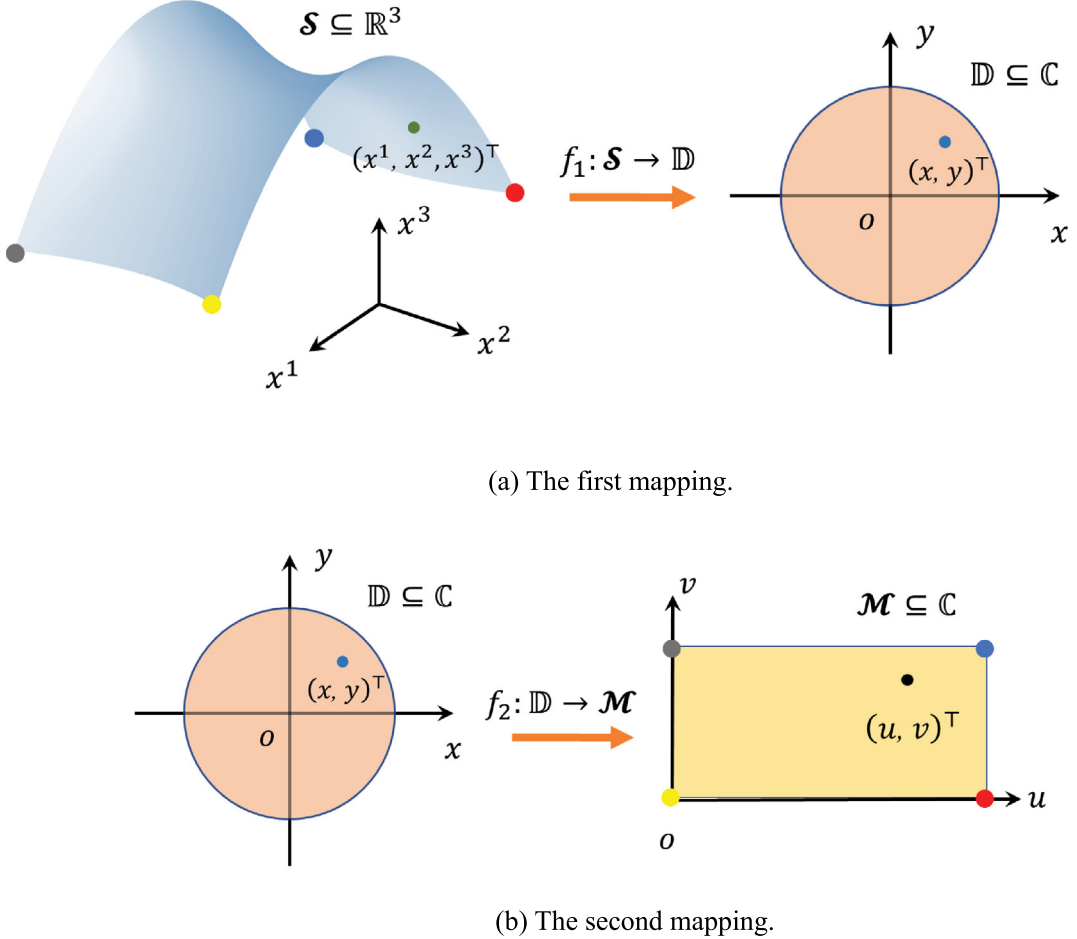


Fig. 3. An illustration of the conformal mapping composed of two quasi-conformal mappings.

the point $\mathbf{P} = (u, v, w)^\top$ on S_0 form a one-to-one mapping relationship. $\mathbf{P}_0 = (u, v, 0)^\top$ and $\mathbf{P}'_0 = (x_0, y_0, z_0)^\top$ are the projection point of point \mathbf{P} on domain \mathcal{M} and the projection point of point \mathbf{P}' on domain \mathcal{S} , respectively. Accordingly, the coordinates of point \mathbf{P}' can be represented by

$$\mathbf{P}' = \mathbf{P}'_0 + wh\mathbf{N}_P, \quad (2.5)$$

where $\mathbf{P}'_0 = f^{-1}(u, v)$ is calculated by \mathbf{P}_0 based on the inverse mapping $f^{-1}: \mathcal{M} \rightarrow \mathcal{S}$ of the conformal mapping and $\mathbf{N}_P(u, v) = (N_{Px}, N_{Py}, N_{Pz})$ denotes the outer normal vector of the surface \mathcal{S} at point \mathbf{P}'_0 . In Eq. (2.5), $w \in [0, 1]$ is a parameter denoting the position along the height direction of the component. Based on the above analysis, the configuration of the mid-surface S'_0 of the component can be formulated as

$$S'_0(u, v, w) = f^{-1}(u, v) + wh\mathbf{N}_P(u, v), \quad (u, v) \in \mathcal{M} \text{ and } w \in [0, 1]. \quad (2.6)$$

Once the mid-surface of the thin-walled component is constructed, any point on the two main outer boundaries S'_1 and S'_2 of the component (see Fig. 6(c)) can be written as follows

$$S'_1(u, v, w) = S'_0(u, v, w) + \frac{t}{2}\mathbf{n}_P^1(u, v), \quad (2.7a)$$

$$S'_2(u, v, w) = S'_0(u, v, w) - \frac{t}{2}\mathbf{n}_P^1(u, v), \quad (2.7b)$$

where \mathbf{n}_P^1 denotes the outward normal vector on boundary S'_1 and it can be calculated in the following form

$$\mathbf{n}_P^1 = (\boldsymbol{\tau}_P \times \mathbf{N}_P). \quad (2.8)$$

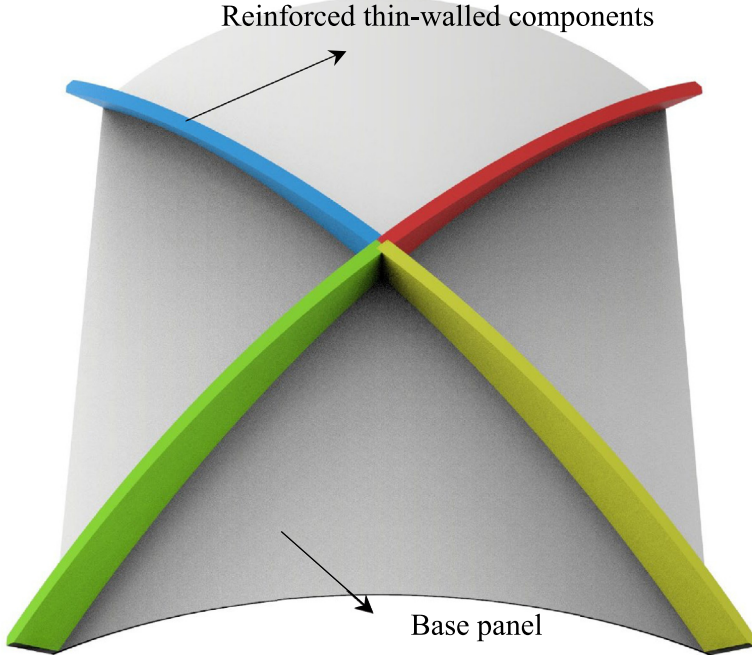
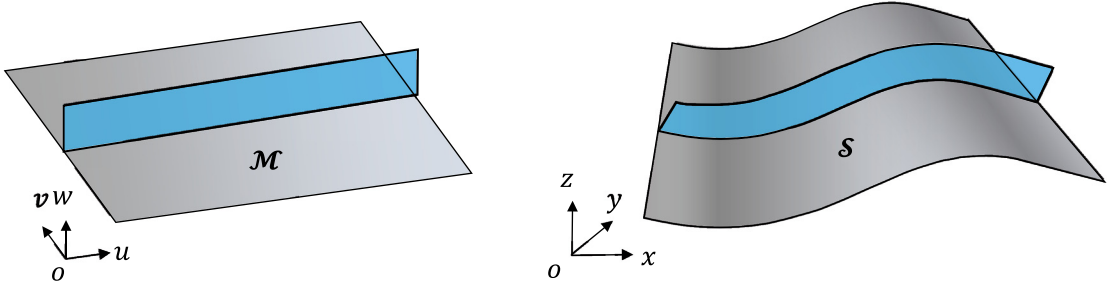


Fig. 4. The geometric model of a rib-reinforced thin-walled structure.



(a) The component in the parameter space.

(b) The component in the physical space.

Fig. 5. Mapping the component from the parameter space to the physical space.

In Eq. (2.8), τ_P represents the tangent vector at the projection point P'_0 of the bottom skeleton of the mid-surface. Based on the above equations, it can be seen that the geometry and position of the thin-walled component in the physical space are totally controlled by the location parameters of the component in the parametric space (i.e., $p_u^1, p_v^1, p_u^2, p_v^2$) and the geometric parameters of the component in the physical space (i.e., h, t).

In the present work, the so-called node-driven adaptive ground structure approach is utilized to design the initial layout of the ribs and regularize the optimization process [48]. The key idea of this approach is to make adjacent ribs driven by common nodes, which effectively prevents overlap and intersection between ribs, and Fig. 7(a) illustrates the initial design of reinforced ribs on a typical simple surface. To avoid overlap between ribs, these driven nodes distributed in the design domain are set to their respective movement ranges, as shown in Fig. 7(b). Nodes located at the vertices of the parameter domain are immobile. Nodes distributed at the boundary of the parameter domain are

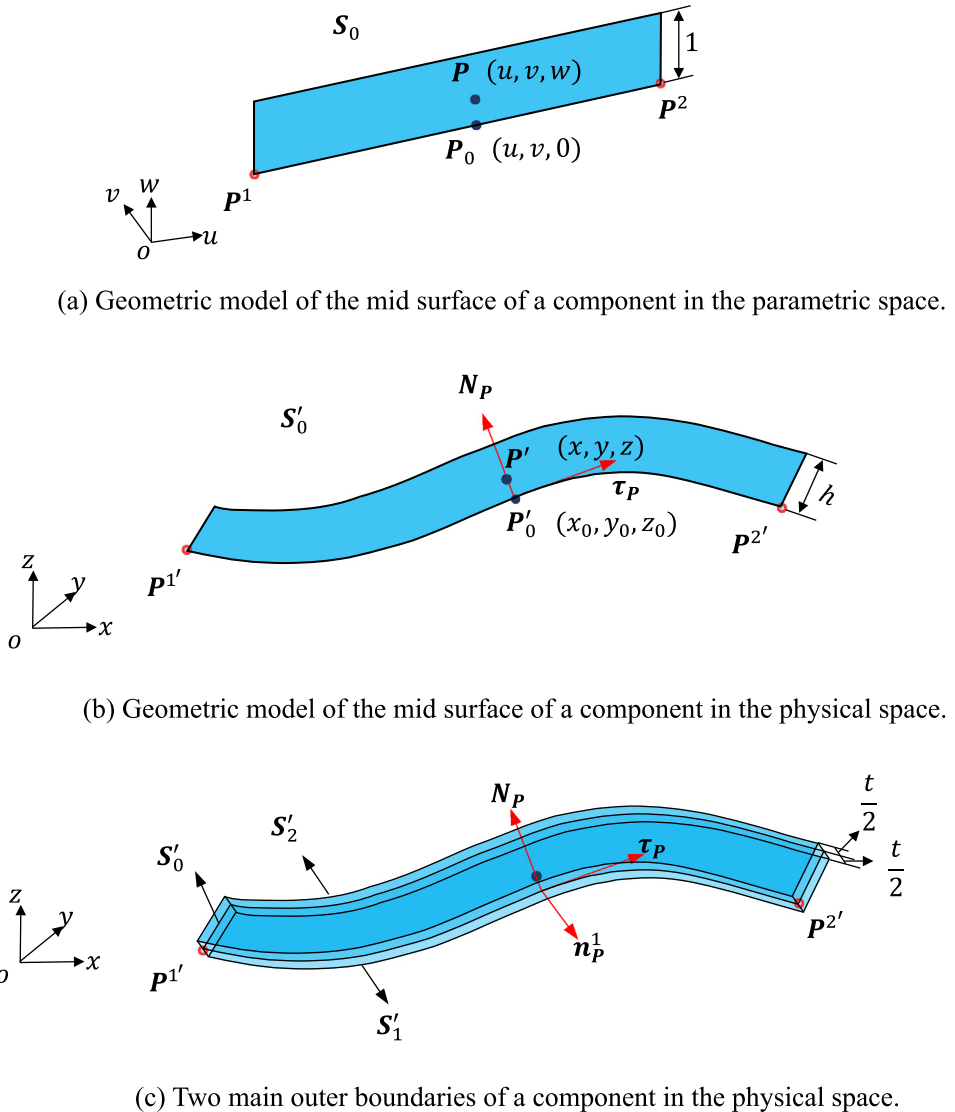
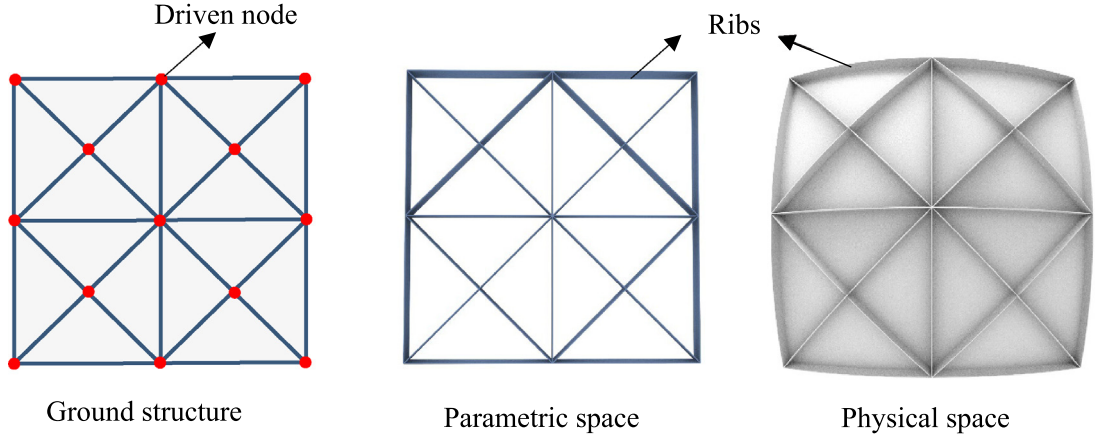


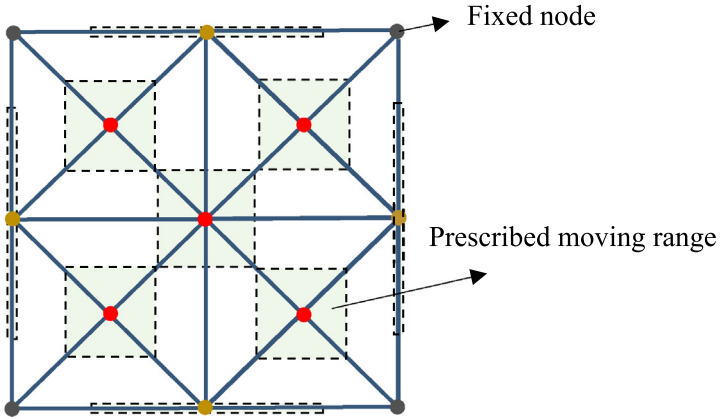
Fig. 6. Construction of a thin-walled component in the physical space.

allowed to move only on the boundary line. Nodes inside the parameter domain can move relatively freely within the rectangular neighborhood of their initial positions. Based on the above definition, the size, shape and layout of the stiffeners can be modified by optimizing the geometric parameters of the components and the coordinates of these driven nodes. Currently, the topology change of the rib-reinforced thin-walled structure can be realized by removing those narrow stiffeners with thickness below a prescribed threshold value from the final optimized result when the optimization process is completed.

At this position, it should be admitted that the proposed method does inherit the property of initial design dependency, which is one of the shortcomings of the ground structure approach. The optimized designs obtained may be more or less affected by the initial layout of ribs. It is worth noting, however, that the proposed method is not the traditional ground structure approach with fixed topology, it is actually an adaptive ground structure approach with movable nodes and components. Under this circumstance, the design freedom can be enlarged and the initial design dependency can be alleviated effectively. On the other hand, we also think that the initial design dependence



(a) A typical initial design for the reinforced ribs.



(b) The specified moving ranges of the driven nodes.

Fig. 7. An illustration of the initial design established by the node-driven adaptive ground structure method.

can also be alleviated as long as a sufficient number of driven nodes and components are introduced in the initial design, and some numerical experiments provided in [48] have also indicated that.

When the topology of the base panel is complex (e.g., a manifold with a high genus), cutting operation is introduced for the definition of parameterization. Taking a torus surface with genus 1 as an example, after cutting along the radial section line Γ_1 and the torus line Γ_2 of the surface, the obtained intermediate surface \mathcal{S}^* can be conformally mapped onto a rectangular plane \mathcal{M} , as shown in Fig. 8(a). Accordingly, the initial rib layout can be set on the parametric plane \mathcal{M} and then mapped onto the torus surface \mathcal{S} . Since the ribs lying on different sides of the cutting line Γ_i may eventually overlap each other in physical space, we only place the ribs on one side of the cut line (Γ'_i) in parameter space (see Fig. 8(b) for reference). Also, the movements of the drive nodes on different sides of the cutting line Γ_i are set to be synchronized during the optimization process. Fig. 8(c) shows the corresponding initial rib layout in the physical space.

Since the global parameterization of a single patch is normally too stiff and causes distortions in geometry modeling, rib optimization may encounter nonlinearity and instability. To tackle this problem, the commonly used multi-patch stitching technique [42,49–51] is introduced to decrease the distortion of the parametric mapping and

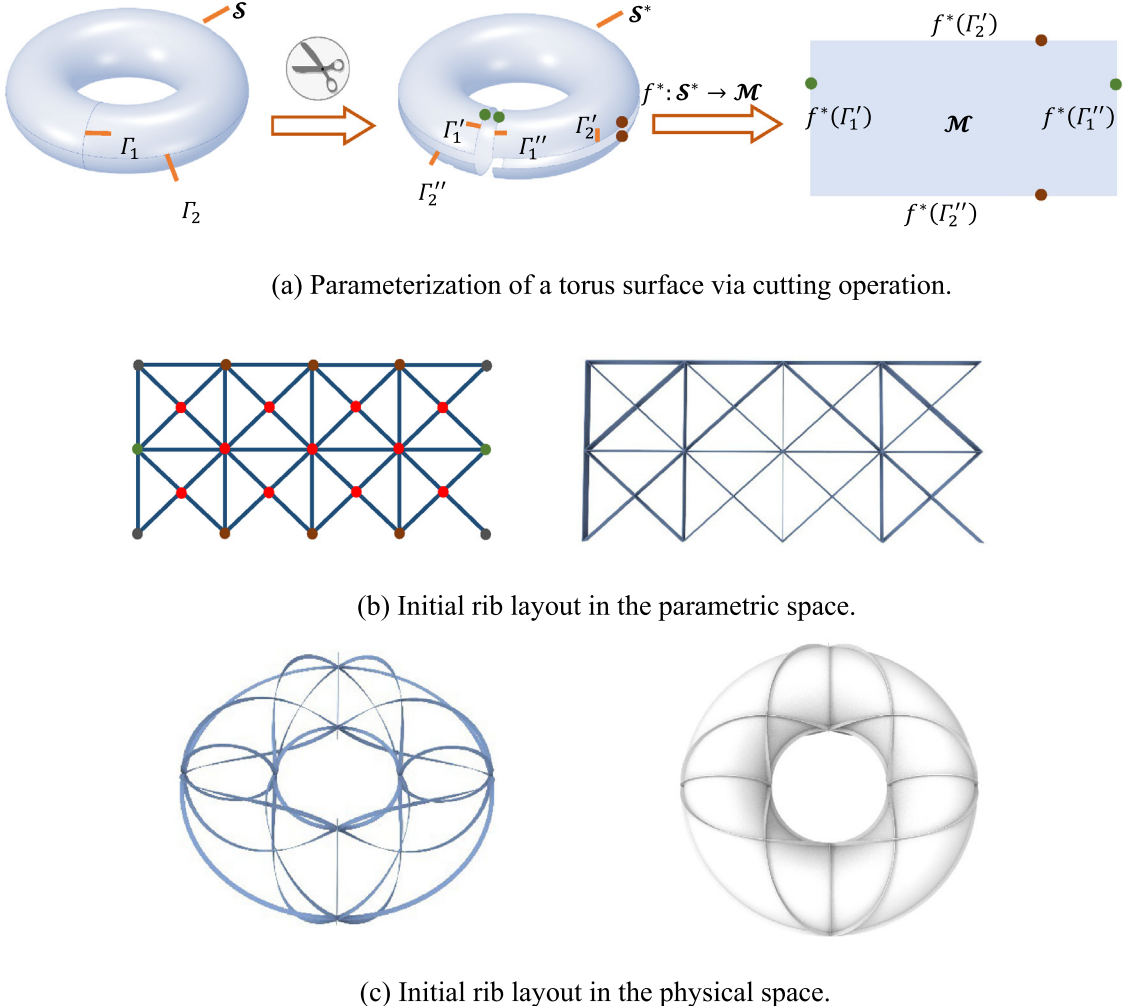


Fig. 8. The parameterization and initial rib layout of a torus surface.

enhance the fidelity of the geometric model of ribs. Here, we show the stitching pattern for a classic surface with a high genus, as depicted in Fig. 9. Once the stitching operation of the surfaces is done, the conformal parameterization mapping and the corresponding rib modeling can be accomplished on each patch using the methods described previously.

3. Problem formulation

The considered optimization problem of this paper is to minimize the compliance of the rib-reinforced thin-walled structure under the constraint of the available volume of the entire reinforced ribs. Both the base panel and the reinforced ribs are modeled by the thin-walled components simulated by highly accurate shell elements. The region occupied by the whole thin-walled structure is represented as $\mathcal{B} = \bigcup_{i=0}^{nc} \mathcal{B}_i$, where \mathcal{B}_0 denotes the base panel (fixed) and \mathcal{B}_i for $i = 1, 2, \dots, nc$ are the regions occupied by nc components (to be designed). It is assumed that \mathcal{B}_i is parameterized by a bijective mapping $\bar{\varphi}_i$ from the parametric space $\Omega_i = \omega_i \times (-\frac{t_i}{2}, \frac{t_i}{2}) = \left\{ \xi = (\xi^1, \xi^2, \xi^3) \mid (\xi^1, \xi^2) \in \omega_i, \xi^3 \in \left(-\frac{t_i(\xi^1, \xi^2)}{2}, \frac{t_i(\xi^1, \xi^2)}{2} \right) \right\}$ such that $\mathcal{B}_i = \bar{\varphi}_i(\Omega_i)$ and $\mathcal{S}_i = \varphi_i(\omega) = \bar{\varphi}_i(\omega_i \times (\xi^3 = 0))$ is the mid-surface of \mathcal{B}_i . Note that $\bar{\varphi}_i(i = 1, \dots, nc)$ is controlled by the coordinates of the driven nodes of the i th component and other geometric parameters. Accordingly, the design

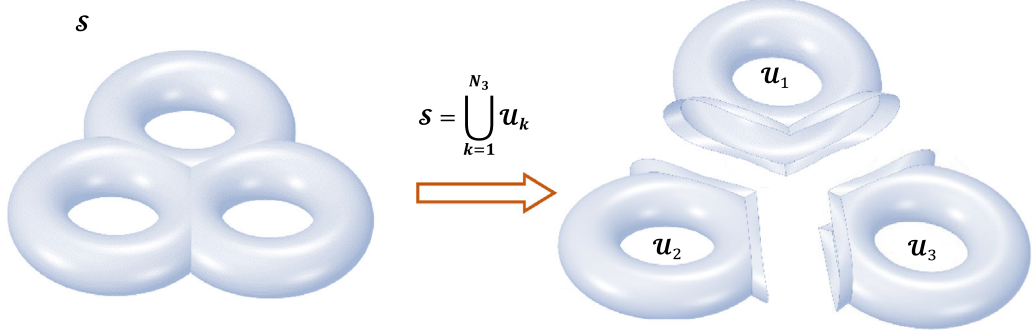


Fig. 9. The multi-patch stitching operation of a complex surface.

variables of the rib-reinforced thin-walled structure optimization problem can be expressed by an integrated vector composed of the coordinates of all driven nodes (i.e., $\mathbf{D}_P = ((\mathbf{P}^1)^\top, \dots, (\mathbf{P}^j)^\top, \dots, (\mathbf{P}^{nn})^\top)^\top$, where nn denotes the total number of the driven nodes) and other geometric parameters of all components (i.e., $\mathbf{D}_S = ((S^1)^\top, \dots, (S^k)^\top, \dots, (S^{nc})^\top)^\top$). It is worth noting that the height of the rib is assumed to be constant in the present work. Actually, taking the height of the rib into consideration has no intrinsic difficulty in the proposed method. It only needs to include the rib's height in the vector of design variables and perform the corresponding sensitivity analysis. Since the main purpose of the present work is to demonstrate the applicability of the proposed method for optimizing rib-reinforced thin-walled structures with complex middle surfaces, we intend to explore the effect of height on improving the performance of rib-reinforced thin-wall structures systematically in future work.

Under the above circumstance, the corresponding layout optimization problem can be formulated mathematically in the following form:

$$\text{Find } \mathbf{U} = (\mathbf{U}^1, \dots, \mathbf{U}^i, \dots, \mathbf{U}^{nc}), \mathbf{D} = (\mathbf{D}_P, \mathbf{D}_S) \quad (3.1a)$$

$$\text{Minimize } I = I(\mathbf{U}(\mathbf{D}), \mathbf{D}) = \sum_{i=0}^{nc} \int_{-\frac{t_i(\xi^1, \xi^2)}{2}}^{\frac{t_i(\xi^1, \xi^2)}{2}} \int_{\omega_i} (\mathbf{F}^i \cdot \mathbf{U}^i) \sqrt{g_i} d\xi^1 d\xi^2 d\xi^3, \quad (3.1b)$$

s.t.

$$\begin{aligned} & \sum_{i=0}^{nc} \int_{-t_i(\xi^1, \xi^2)/2}^{t_i(\xi^1, \xi^2)/2} \int_{\omega_i} \left(\mathcal{C}_i^{\alpha\beta\lambda\mu} e_{\alpha\beta}(\mathbf{U}^i) e_{\lambda\mu}(\mathbf{V}^i) + \mathcal{D}_i^{\alpha\lambda} e_{\alpha 3}(\mathbf{U}^i) e_{\lambda 3}(\mathbf{V}^i) \right) \sqrt{g_i} d\xi^1 d\xi^2 d\xi^3 \\ &= \sum_{i=0}^{nc} \int_{-\frac{t_i(\xi^1, \xi^2)}{2}}^{\frac{t_i(\xi^1, \xi^2)}{2}} \int_{\omega_i} (\mathbf{F}^i \cdot \mathbf{V}^i) \sqrt{g_i} d\xi^1 d\xi^2 d\xi^3, \forall \mathbf{V} = (\mathbf{V}^1, \dots, \mathbf{V}^i, \dots, \mathbf{V}^{nc}) \in U_{ad}^1 \times \dots \times U_{ad}^{nc}, \end{aligned} \quad (3.1c)$$

$$\sum_{i=1}^{nc} \int_{-\frac{t_i(\xi^1, \xi^2)}{2}}^{\frac{t_i(\xi^1, \xi^2)}{2}} \int_{\omega_i} \sqrt{g_i} d\xi^1 d\xi^2 d\xi^3 - \bar{V} \leq 0, \quad (3.1d)$$

$$\mathbf{U}^i \in \mathcal{U}_u^i, i = 0, \dots, nc, \quad (3.1e)$$

$$\mathbf{D} \in \mathcal{U}_D. \quad (3.1f)$$

In Eq. (3.1), $\mathbf{U}^i = \mathbf{U}^i(\mathbf{u}^i, \boldsymbol{\theta}^i)$ and $\mathbf{V}^i = \mathbf{V}^i(\mathbf{v}^i, \boldsymbol{\eta}^i)$ represent the primary displacement field and the corresponding virtual displacement associated with the i th region, respectively. $\mathbf{U}^i = \mathbf{U}^i(\mathbf{u}^i, \boldsymbol{\theta}^i)$ belongs to a prescribed constraint set \mathcal{U}_u^i and $\mathbf{V}^i = \mathbf{V}^i(\mathbf{v}^i, \boldsymbol{\eta}^i)$ belongs to an admissible set U_{ad}^i . The specific mathematical form of \mathbf{U}^i and \mathbf{V}^i can be expressed as follows [52]

$$\mathbf{U}^i = \mathbf{U}^i(\xi^1, \xi^2, \xi^3) = \mathbf{u}^i(\xi^1, \xi^2) + \xi^3 \theta_\lambda^i(\xi^1, \xi^2) (\mathbf{a}^\lambda)^i(\xi^1, \xi^2), \quad (3.2a)$$

$$\mathbf{V}^i = \mathbf{V}^i(\xi^1, \xi^2, \xi^3) = \mathbf{v}^i(\xi^1, \xi^2) + \xi^3 \eta_\lambda^i(\xi^1, \xi^2) (\mathbf{a}^\lambda)^i(\xi^1, \xi^2), \quad (3.2b)$$

where $(\mathbf{a}^\lambda)^i$, $\lambda = 1, 2, 3$ denote the contravariant base vectors, which are associated with the covariant base vectors $\mathbf{a}_\alpha^i = \partial\varphi_i/\partial\xi^\alpha$, $\alpha = 1, 2$ and $\mathbf{a}_3^i = (\mathbf{a}_1^i \times \mathbf{a}_2^i)/\|\mathbf{a}_1^i \times \mathbf{a}_2^i\|$. In Eq. (3.1b) and Eq. (3.1c), $\mathbf{F}^i = \mathbf{F}^i(\xi^1, \xi^2, \xi^3)$ represents the external load on \mathcal{B} , $\mathcal{C}_i = (\mathcal{C}_i^{\alpha\beta\lambda\mu})$ and $\mathcal{D}_i = (\mathcal{D}_i^{\alpha\lambda})$ denote the modified constitutive tensors of the linear elastic material composed of the i th region expressed in the convected curvilinear coordinate system (ξ^1, ξ^2, ξ^3) . Furthermore, $e_{\alpha\beta}(\mathbf{U}^i)$ ($e_{\alpha\beta}(\mathbf{V}^i)$) and $e_{\alpha 3}(\mathbf{U}^i)$ ($e_{\alpha 3}(\mathbf{V}^i)$) denote the surface and transverse shear strain tensors corresponding to the primary (virtual) displacement, respectively. The specific forms of $e_{\alpha\beta}$ and $e_{\alpha 3}$ depend on the shell theory adopted. In addition, the quantity $\sqrt{g_i}$ in Eq. (3.1c) and Eq. (3.1d) takes the form of $\sqrt{g_i} = |\mathbf{g}_1^i \cdot (\mathbf{g}_2^i \times \mathbf{g}_3^i)|$ with $\mathbf{g}_\alpha^i = \partial\varphi_i/\partial\xi^\alpha$, $\alpha = 1, 2, 3$. For details, readers can refer to [52] for more information on the variational formulation for shell analysis. Lastly, the symbol \bar{V} in Eq. (3.1d) is the upper bound of the available material volume of ribs and \mathcal{U}_D in Eq. (3.1f) represents the admissible set of \mathbf{D} .

4. Numerical solution aspects

4.1. Finite element analysis

Considering the accuracy and efficiency of the analysis results, the base panel and the reinforced ribs are discretized to triangular S3 shell elements and quadrilateral S4R shell elements (see Fig. 10), respectively, and these elements are classic stress/displacement shell elements which are built from a refined shell theory [53]. In the present work, the mesh of the base panel is fixed after mesh generation, while the mesh of the reinforced ribs is constructed by the adaptive meshing technique and updated in each iteration loop. Consequently, to ensure the connection between the base panel and the ribs, nodal displacement constraint equations are adopted to establish the displacement compatible conditions. Suppose \mathbf{P}_r is a node at the bottom of the rib mesh, which is also located on an element of the surface mesh (as shown in Fig. 10), the corresponding constraint equation is of the following form

$$\mathbf{U}_{\mathbf{P}_r} = N_{bi}\mathbf{U}_{\mathbf{P}_{bi}} + N_{bj}\mathbf{U}_{\mathbf{P}_{bj}} + N_{bk}\mathbf{U}_{\mathbf{P}_{bk}}, \quad (4.1)$$

where $\mathbf{U}_{\mathbf{P}_r}$, $\mathbf{U}_{\mathbf{P}_{bi}}$, $\mathbf{U}_{\mathbf{P}_{bj}}$ and $\mathbf{U}_{\mathbf{P}_{bk}}$ denote the nodal displacement vectors of nodes \mathbf{P}_r , \mathbf{P}_{bi} , \mathbf{P}_{bj} and \mathbf{P}_{bk} , respectively. In Eq. (4.1), N_{bi} , N_{bj} and N_{bk} are the shape functions of nodes \mathbf{P}_{bi} , \mathbf{P}_{bj} and \mathbf{P}_{bk} established from the global coordinate systems of the element.

It should be pointed out that the above mesh model is essentially established from a series of explicit geometric parameters of the thin-walled components, which makes this model have clear geometric features and can be easily transferred between the CAD and the CAE systems. In addition, compared to the 3D solid model and smeared-out model, the full-shell model can acquire more accurate analysis results of rib-reinforced thin-walled structures at a relatively low computational cost.

4.2. Sensitivity analysis

As mentioned in [48], the proposed rib layout optimization framework for thin-walled structures is actually a boundary-evolution-type method, hence the shape sensitivity analysis method can be employed to calculate the sensitivities of a general objective/constraint functional. According to [54,55], the basic integral form of shape sensitivity can be expressed as

$$\delta I = \int_{\partial\mathcal{B}} \varphi(\mathbf{U}, \mathbf{V}) V_n dS = \sum_{i=1}^{nc} \int_{\partial\mathcal{B}_i \cap \partial\mathcal{B}} \varphi(\mathbf{U}, \mathbf{V}) V_n^i dS. \quad (4.2)$$

In Eq. (4.2), $\partial\mathcal{B}_i$ is the outer boundary of i th reinforced rib and $\partial\mathcal{B} = \partial(\cup_{i=1}^{nc} \mathcal{B}_i)$ denotes the outer boundary of all reinforced ribs. V_n^i represents the outer normal velocity field along boundary $\partial\mathcal{B}_i \cap \partial\mathcal{B}$. In addition, φ is a measure of the structural response. Specifically, when the symbol I denotes the structural compliance, it yields that $\varphi = -2\omega$ with ω representing the strain energy density. When I denotes the volume of all reinforced ribs, we have $\varphi = 1$.

In the following, we take a reinforced rib as an example (see Fig. 6 for reference) and elaborate on the calculation of the outer normal velocity field V_n^i . For the i th rib, V_n^i is associated with the variation of the two main outer boundaries S'_1 and S'_2 , and it can be written as

$$V_n^i = \begin{cases} \delta S'_1 \cdot \mathbf{n}_P^1, & \text{if } (x, y, z) \in S'_1, \\ \delta S'_2 \cdot (-\mathbf{n}_P^1), & \text{if } (x, y, z) \in S'_2. \end{cases} \quad (4.3)$$

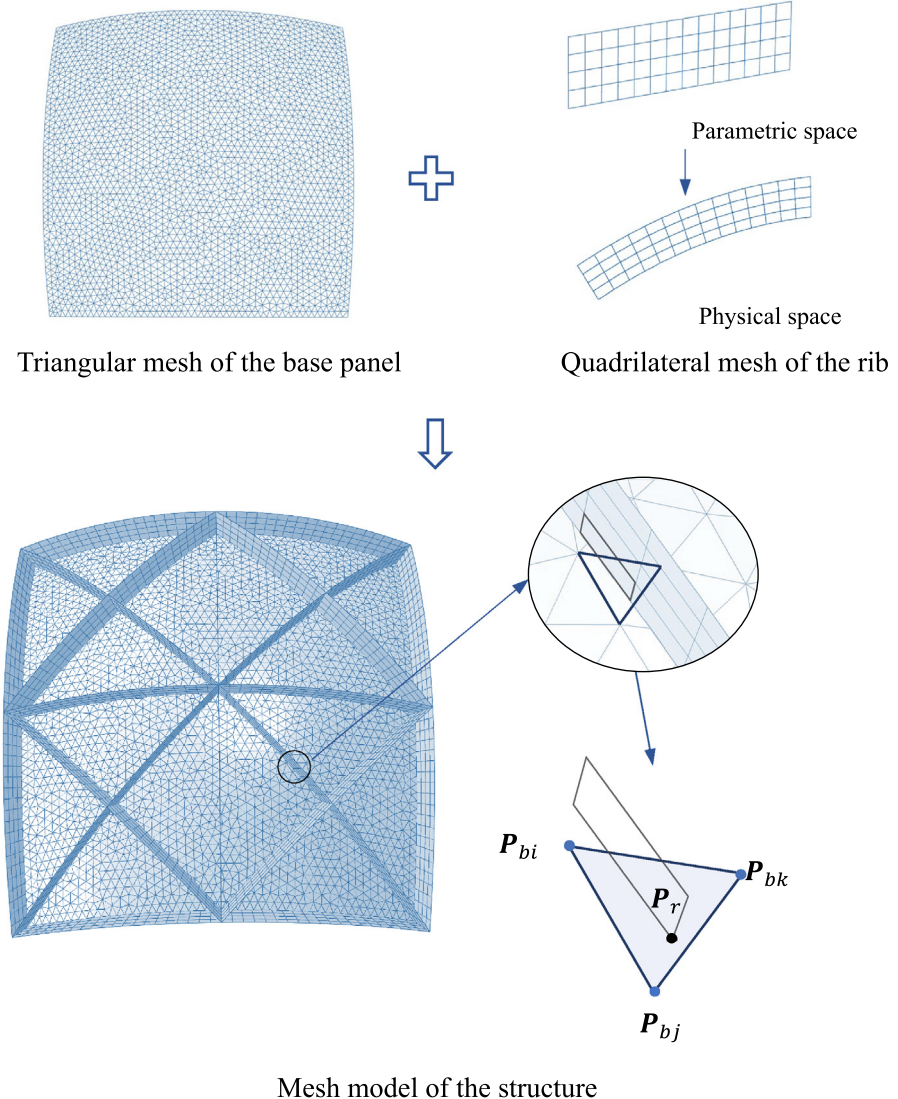


Fig. 10. An illustration of the FE model of a rib-reinforced thin-walled structure.

According to Eq. (2.7), the above equation can be simplified as

$$V_n^i = \begin{cases} \delta S'_0 \cdot \mathbf{n}_P^1 + \frac{\delta t}{2}, & \text{if } (x, y, z) \in S'_1, \\ -\delta S'_0 \cdot \mathbf{n}_P^1 + \frac{\delta t}{2}, & \text{if } (x, y, z) \in S'_2. \end{cases} \quad (4.4)$$

In Eq. (4.4), $\delta S'_0$ can be obtained through Eqs. (2.2) and (2.6) as

$$\begin{aligned} \delta S'_0 &= \frac{\partial S'_0}{\partial u} \delta u + \frac{\partial S'_0}{\partial v} \delta v + \frac{\partial S'_0}{\partial w} \delta w \\ &= \left(\frac{\partial f^{-1}(u, v)}{\partial u} + wh \frac{\partial N_P(u, v)}{\partial u} \right) ((1 - \mu) \delta P_u^1 + \mu \delta P_u^2) \\ &\quad + \left(\frac{\partial f^{-1}(u, v)}{\partial v} + wh \frac{\partial N_P(u, v)}{\partial v} \right) ((1 - \mu) \delta P_v^1 + \mu \delta P_v^2), \end{aligned} \quad (4.5)$$

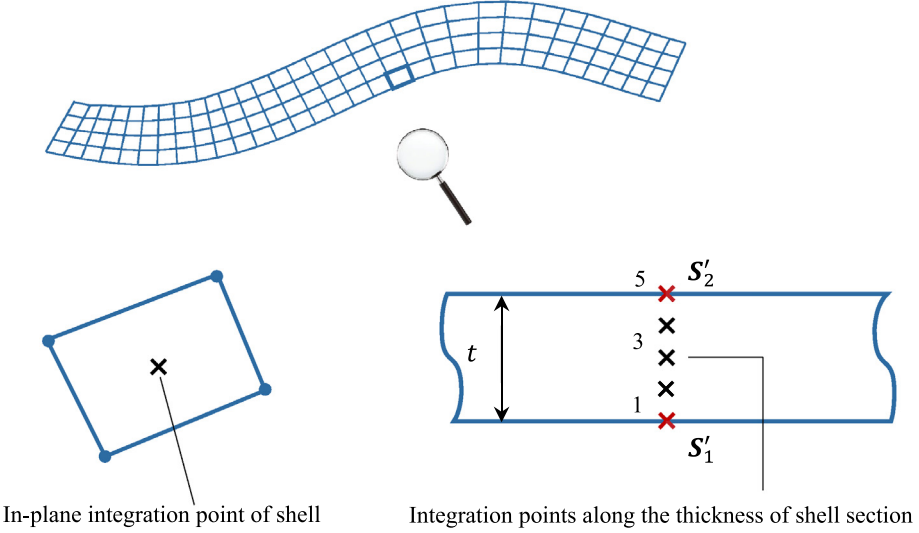


Fig. 11. Numerical integration points of the shell element of the rib.

and \mathbf{n}_P^1 can be calculated using Eq. (2.8). Thus, it can be obtained that

$$V_n^i = \begin{cases} A\delta P_u^1 + B\delta P_u^2 + C\delta P_v^1 + D\delta P_v^2 + \frac{\delta t}{2}, & \text{if } (x, y, z) \in S'_1, \\ -A\delta P_u^1 - B\delta P_u^2 - C\delta P_v^1 - D\delta P_v^2 + \frac{\delta t}{2}, & \text{if } (x, y, z) \in S'_2, \end{cases} \quad (4.6)$$

where the expressions of A , B , C and D can be calculated as

$$A = (1 - \mu) \left(\frac{\partial f^{-1}(u, v)}{\partial u} + wh \frac{\partial N_P(u, v)}{\partial u} \right) \cdot (\boldsymbol{\tau}_P \times \mathbf{N}_P), \quad (4.7a)$$

$$B = \mu \left(\frac{\partial f^{-1}(u, v)}{\partial u} + wh \frac{\partial N_P(u, v)}{\partial u} \right) \cdot (\boldsymbol{\tau}_P \times \mathbf{N}_P), \quad (4.7b)$$

$$C = (1 - \mu) \left(\frac{\partial f^{-1}(u, v)}{\partial v} + wh \frac{\partial N_P(u, v)}{\partial v} \right) \cdot (\boldsymbol{\tau}_P \times \mathbf{N}_P), \quad (4.7c)$$

$$D = \mu \left(\frac{\partial f^{-1}(u, v)}{\partial v} + wh \frac{\partial N_P(u, v)}{\partial v} \right) \cdot (\boldsymbol{\tau}_P \times \mathbf{N}_P). \quad (4.7d)$$

Based on the above equations, the specific forms of sensitivities can be finally summarized as

$$\frac{\partial I}{\partial P_u^1} = \sum_{i=1}^{np_1} \left(\int_{S'_1^i} A\varphi(\mathbf{U}, \mathbf{V}) dS - \int_{S'_2^i} A\varphi(\mathbf{U}, \mathbf{V}) dS \right), \quad (4.8a)$$

$$\frac{\partial I}{\partial P_u^2} = \sum_{i=1}^{np_1} \left(\int_{S'_1^i} B\varphi(\mathbf{U}, \mathbf{V}) dS - \int_{S'_2^i} B\varphi(\mathbf{U}, \mathbf{V}) dS \right), \quad (4.8b)$$

$$\frac{\partial I}{\partial P_v^1} = \sum_{i=1}^{np_2} \left(\int_{S'_1^i} C\varphi(\mathbf{U}, \mathbf{V}) dS - \int_{S'_2^i} C\varphi(\mathbf{U}, \mathbf{V}) dS \right), \quad (4.8c)$$

$$\frac{\partial I}{\partial P_v^2} = \sum_{i=1}^{np_2} \left(\int_{S'_1^i} D\varphi(\mathbf{U}, \mathbf{V}) dS - \int_{S'_2^i} D\varphi(\mathbf{U}, \mathbf{V}) dS \right), \quad (4.8d)$$

$$\frac{\partial I}{\partial t} = \frac{1}{2} \int_{S'_1 + S'_2} \varphi(\mathbf{U}, \mathbf{V}) dS, \quad (4.8e)$$

where np_1 and np_2 denote the total number of the reinforced ribs controlled by driven nodes P^1 and P^2 , respectively. It is worthwhile to point out that the above calculations can be implemented easily by integrals on the boundary of the shell elements of each reinforced rib. As shown in Fig. 11, five numerical integration points are set along the

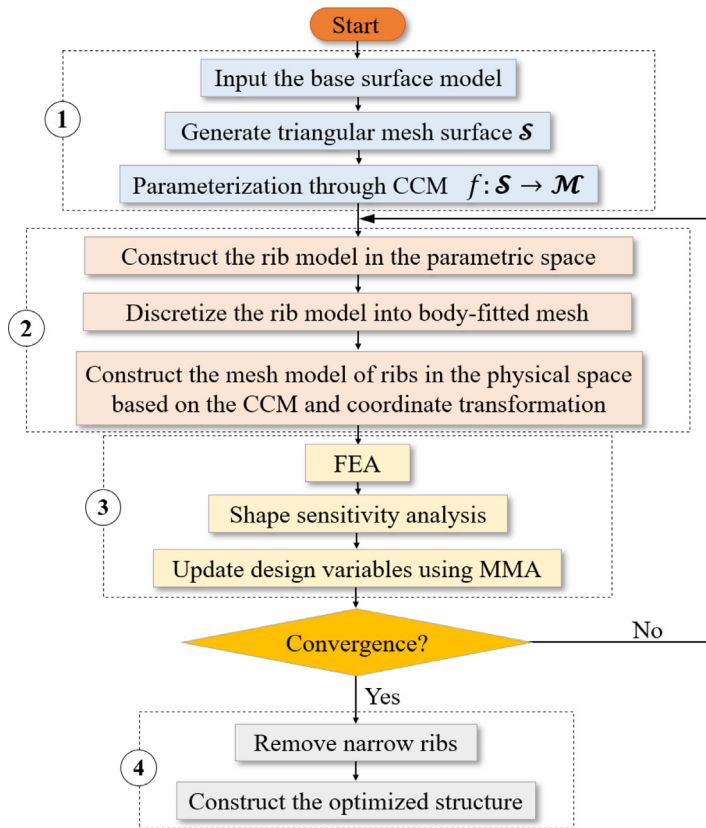


Fig. 12. Flowchart of the optimization procedure.

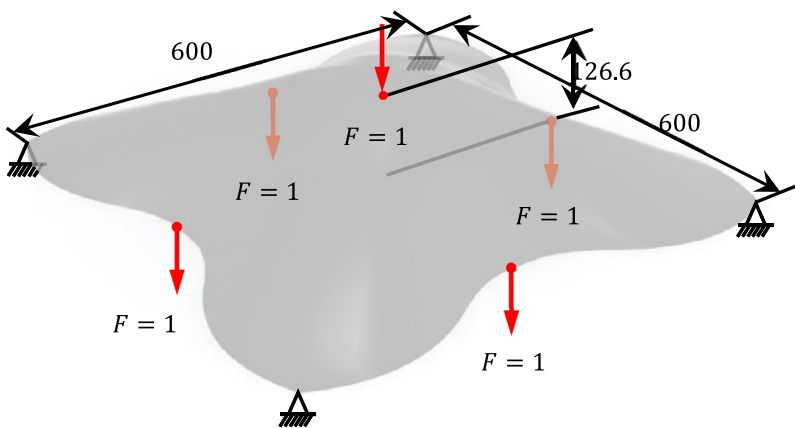


Fig. 13. The rib-reinforced blunt shell example.

thickness direction of the shell element, in which integration points 1 and 5 are used to calculate the integration quantity on the outer boundary S'_1 and S'_2 , respectively.

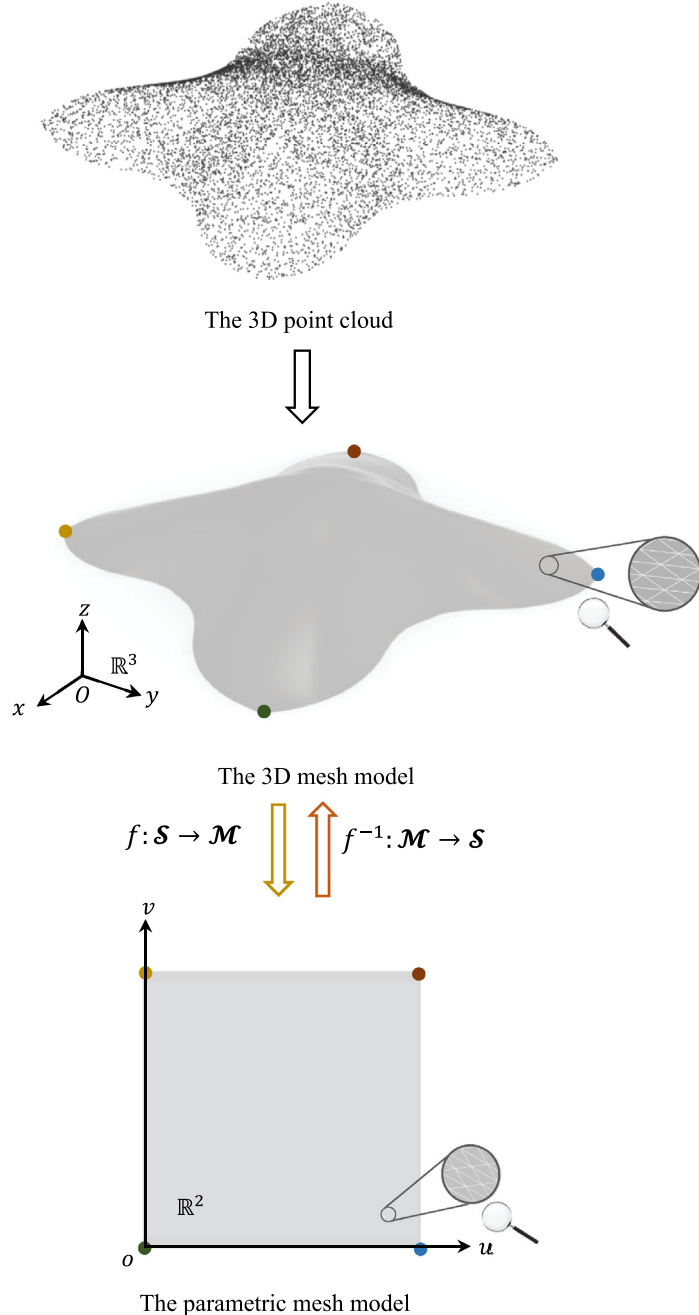


Fig. 14. Parameterization of the input model of the rib-reinforced blunt shell example.

4.3. Optimization procedure

Under the proposed optimization framework, the corresponding optimization procedure for the layout design of rib-reinforced thin-walled structures is concluded in Fig. 12. It mainly contains four flows, namely the parameterization of the base surface, the establishment of the rib model, the solution of the optimization process and the output/post-processing of the optimized results. Firstly, the 3D triangular mesh surface \mathcal{S} is generated

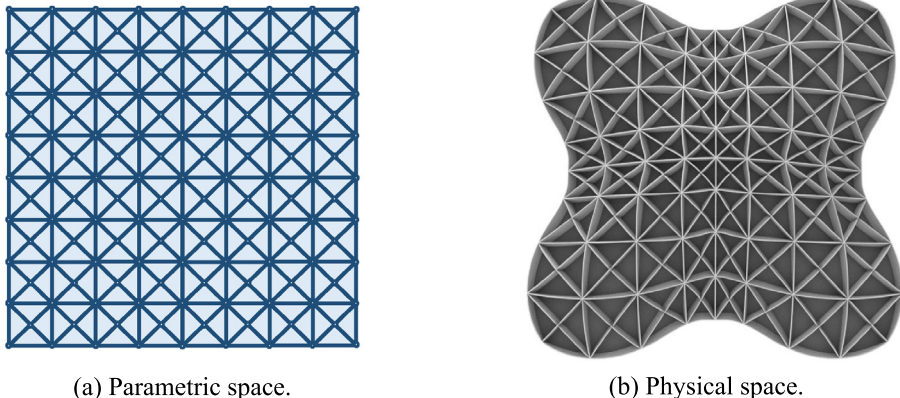


Fig. 15. The initial rib layout of the rib-reinforced blunt shell example.

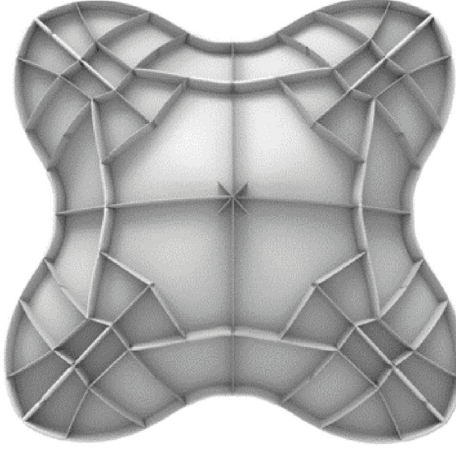
from the input base surface model. Parameterization mapping f from \mathcal{S} to \mathcal{M} is further constructed by means of the computational conformal mapping approach. In the flow of establishing the rib model, the rib model is first constructed in the parametric space and discretized into body-fitted shell mesh via the adaptive meshing technique. Then the coordinate transformation of the nodes of the rib mesh model in the parametric space is implemented to obtain the rib mesh model in the physical space. Once the FE model of the entire rib-reinforced thin-walled structure is established, the optimization process, including the finite element analysis, shape sensitivity analysis and update of design variables, is performed. Flow 2 and 3 are repeated until the convergence criterion is satisfied. Eventually, the optimized structure is obtained by removing those narrow ribs with thickness less than a specified threshold from the optimization results of the last step.

5. Numerical examples

In this section, the effectiveness of the proposed rib layout optimization method for thin-walled structures with complex surfaces is validated by several numerical examples. Firstly, a rib-reinforced blunt shell example, which is a typical single-patch thin-walled structure, is studied and compared. Then, the proposed method is applied to deal with the optimization design of topologically complex rib-reinforced thin-walled structures, including a rib-reinforced torus-shaped shell with a non-zero genus, a rib-reinforced flower-shaped shell and a rib-reinforced tee-branch pipe with multi patches. Note that the involved geometry data, material properties and external loads of all examples are assumed to be dimensionless for illustration purposes. The Young's modulus of the base shell and the reinforced ribs are chosen as $E_b = 1$ and $E_r = 2$, respectively and the Poisson's ratio of the solid material is assumed as $\nu = 0.3$. In all examples, triangular meshes and quadrilateral meshes are adopted for finite element analysis of the base shell and the reinforced ribs, respectively. In addition, the reinforced ribs are discretized into shell elements and updated by using the adaptive re-meshing technique at each iteration step. The method of moving asymptotes (MMA) [56] is chosen as the numerical optimizer. If the relative change in the value of each design variable between two successive iterations is less than a threshold value of $Tol = 0.01$, the optimization process is terminated.

5.1. A rib-reinforced blunt shell example

In the first example, we concentrate on the rib layout optimization problem of a typical rib-reinforced blunt shell structure with the base surface formed by a single patch. As depicted in Fig. 13, five vertical unit loads are applied on the base shell surface and four corners of the shell are simply fixed. The height of all ribs to be optimized is set to a constant value $h_r = 20$ and the thickness of the base shell surface is set as $t_b = 3$. The available rib volume is set to no more than 6% of the volume of the design domain (the volume of the design domain can be computed by $|D| = s_b \times h_r$ with s_b denoting the area of the base shell surface).



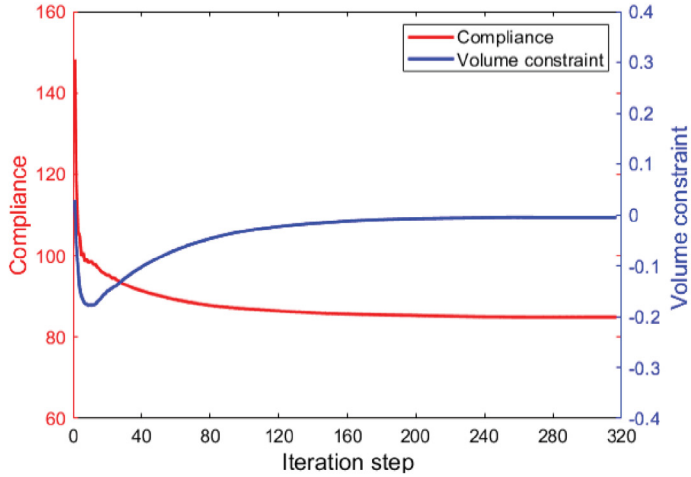
(a) By computational conformal mapping technique ($C^{opt} = 84.86$).



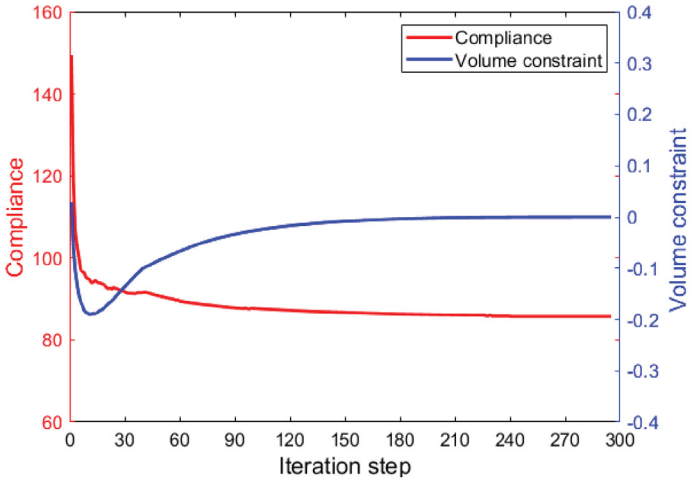
(b) By NURBS parameterization technique ($C^{opt} = 85.68$) [48].

Fig. 16. The optimized designs by using different methods for the rib-reinforced blunt shell example.

It should be emphasized that our proposed method has the capability of dealing with different types of input models, such as the point cloud model, CAD model and mesh model. With the help of 3D scanning techniques, the geometry data of this example, which consists of a series of 3D points and is exported into a standard Polygon (PLY) format [57], is first generated via the scanning of the base surface panel. Further, triangular mesh models can be generated directly from the exported PLY data and there are totally 35 378 meshes. Once the triangular mesh surface is constructed, parameterization of the triangular mesh surface is implemented by means of the computational conformal mapping technique. Since the genus of the base surface is 0, a parametric plan rectangle is obtained without resorting to cutting operations. Fig. 14 manifests the complete procedures for parameterizing the input model of this example. The initial rib layout is composed of 400 thin-walled components and 145 driven nodes, which are first built in the parametric space and then mapped to physical space (see Fig. 15). The coordinates of these driven nodes and the thickness of all ribs are served as design variables, and the total number of design



(a) By computational conformal mapping technique.

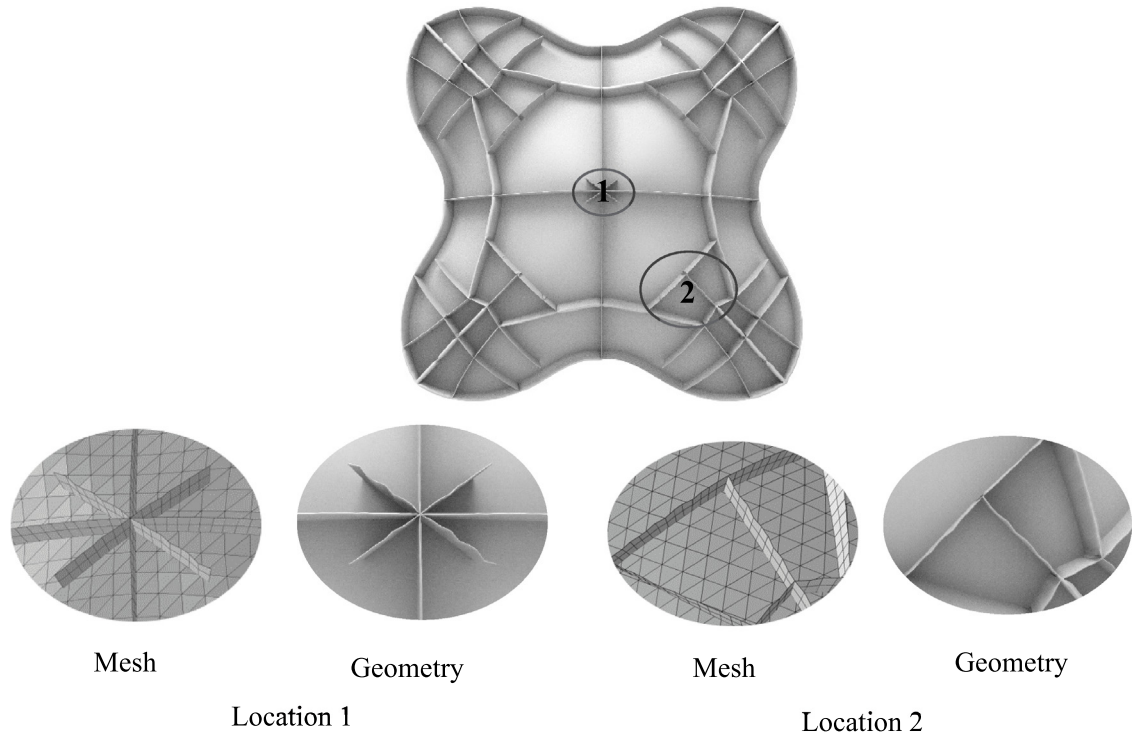


(b) By NURBS parameterization technique.

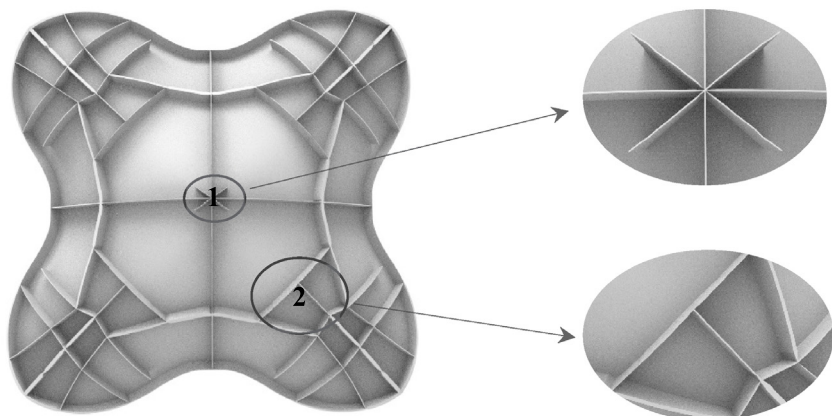
Fig. 17. The iteration histories of the rib-reinforced blunt shell example.

variables for this example is 654. The thickness of each rib (with initial value $t = 1$) is specified to vary within the range of $[0.001, 6]$ during the optimization process.

The optimized rib design of this example is given in Fig. 16(a). It should be emphasized that those ribs with thickness below the threshold $t_r = 0.1$ have been removed from the optimization results obtained in the last iteration step (these removed components have little effect on the structural compliance/volume). As can be observed, some smooth and clean reinforced ribs that connected to the vertical loads and the fixed supports are distributed on the curved surface. Since the ribs are built based on a rigorous mapping relationship, these ribs can seamlessly fit the geometry of the base panel. Furthermore, the component connection mechanism based on the adaptive ground structure approach effectively avoids the mutual overlap between the ribs and facilitates the generation of clear load transmission paths. For comparison, the optimized structure using the NURBS parameterization method [48] under



(a) Local unsMOOTH ribs in the optimized result obtained in a coarse mesh.



(b) Reconstruction of the optimized result under a fine mesh.

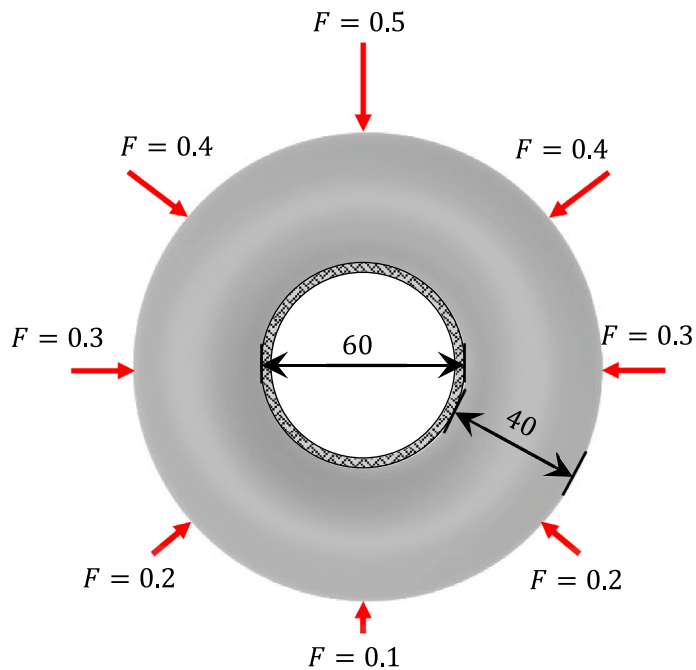
Fig. 18. The optimized results established in different background meshes.

the same problem setting is also provided in Fig. 16(b). It is evident that the results obtained by the two methods are almost identical. Besides, the values of structural compliance of the two optimized results differ by no more than 1%. The corresponding iteration histories of the optimization process for the two methods are depicted in Fig. 17.

Table 1

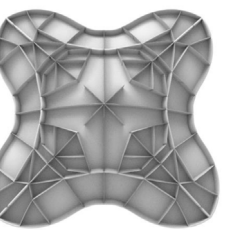
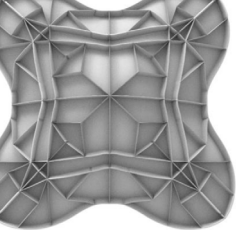
Comparison of the optimized designs with different triangular mesh surfaces.

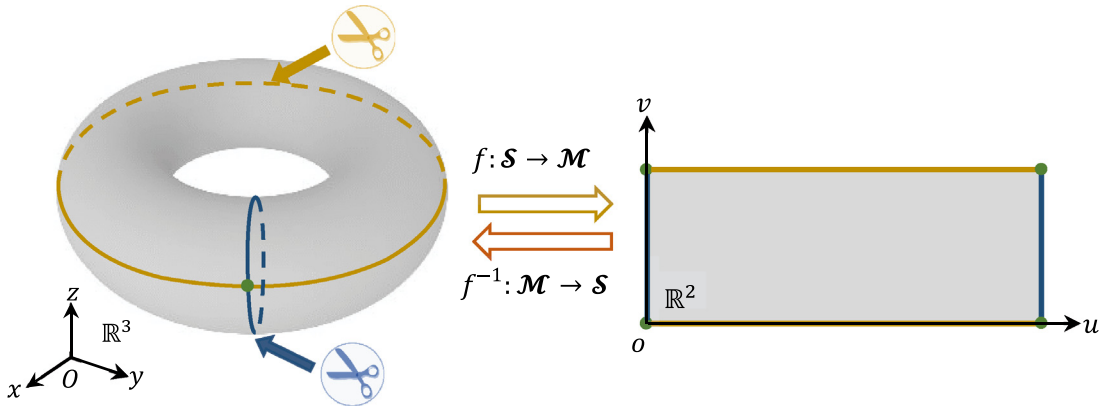
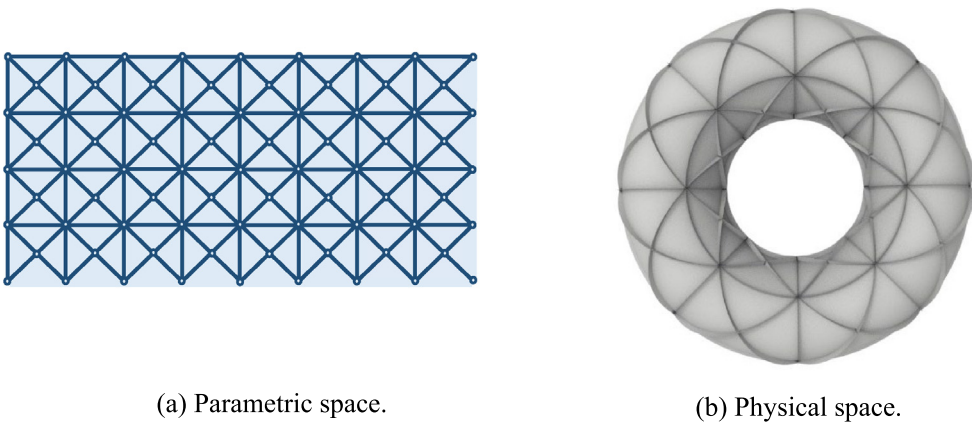
	5000 elements	20,000 elements	35,378 elements	80,000 elements
Iteration step	376	342	317	323
Compliance	84.58	84.65	84.86	85.02
Configuration				

**Fig. 19.** The rib-reinforced torus-shaped shell example.

To test the effect of the mesh density of the surface parameterization on the optimization results, four triangular mesh surfaces with different mesh densities are employed separately to perform parameterization and the subsequent optimization process, while other problem settings remain unchanged. To facilitate comparison, the iteration numbers, compliances values and the corresponding configurations of the optimized designs are listed in **Table 1**. All the optimization processes reach convergence within 400 iteration steps. It can be observed that as the number of surfaces meshes increases, the structural compliance value of the optimized result rises slightly, which is reasonable from a mechanical point of view. In addition, the rib configurations of the four optimized results are very similar, indicating that the optimized results are insensitive to the mesh density of the surface parameterization. However, it should be noticed that the optimized structure reconstructed from the rib mesh model, which is established in a coarse mesh, has locally unsmooth features. This is because the outer normal vector of the surface calculated on a coarse background mesh is not smooth enough (see Fig. 18(a)). The above facts remind us that the optimization procedure can be performed under a coarse background mesh, while the geometry reconstruction of the optimized

Table 2Comparison of the optimized designs with different base panel thickness t_b .

	$t_b = 3$	$t_b = 2$	$t_b = 1$	$t_b = 0.1$
Iteration step	317	331	349	336
Compliance	84.86	102.49	128.18	211.87
Configuration				

**Fig. 20.** Parameterization of the rib-reinforced torus-shaped shell example.**Fig. 21.** The initial rib layout of the rib-reinforced torus-shaped shell example.

result should be carried out from the obtained explicit geometric parameters under a fine background mesh. In this manner, a clear and smooth rib-reinforced thin-walled structure can be finally obtained (see Fig. 18(b)).

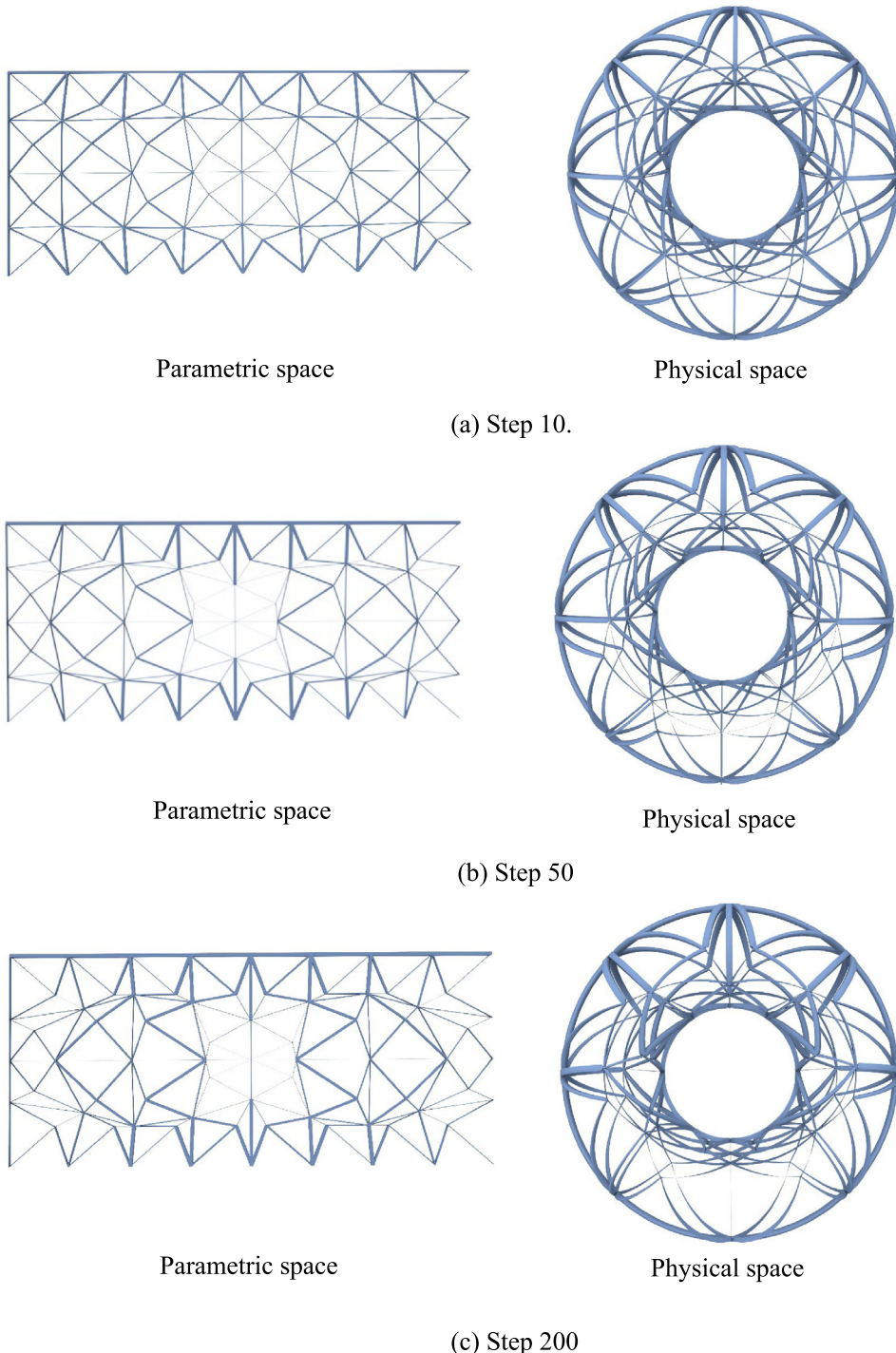


Fig. 22. Some intermediate designs of the rib-reinforced torus-shaped shell example.

Next, we further study the influence of the base panel thickness on the final rib layout. The considered base panel thickness is respectively set to $t_b = 3$, $t_b = 2$, $t_b = 1$ and $t_b = 0.1$ respectively. The corresponding iteration numbers, compliance values and the optimized designs are provided in [Table 2](#). Notice that the rib layouts of the

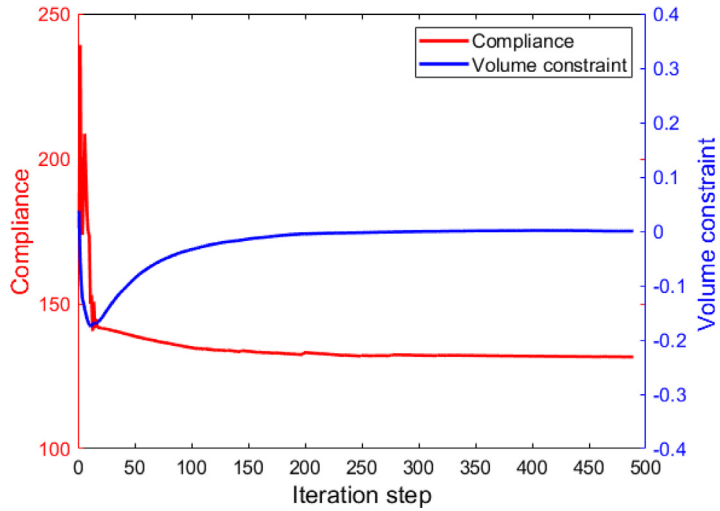


Fig. 23. The iteration history of the rib-reinforced torus-shaped shell example.

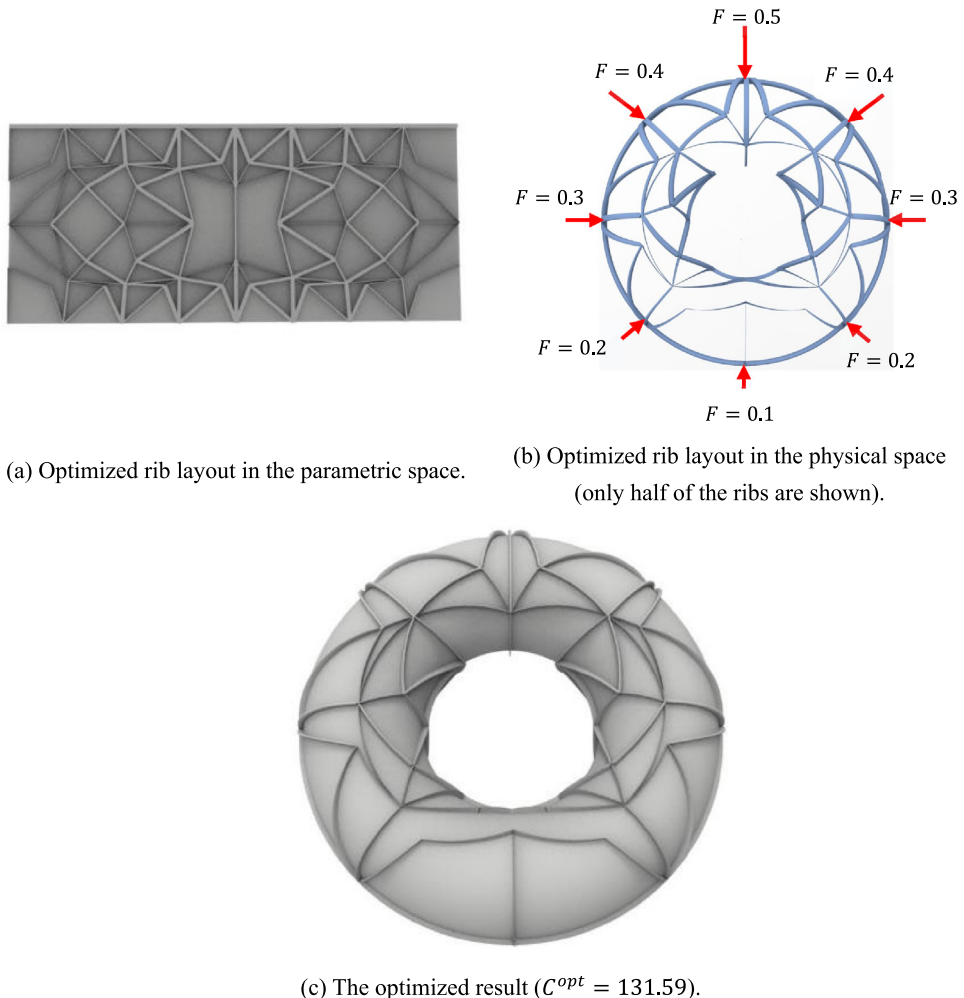


Fig. 24. The optimized design of the rib-reinforced torus-shaped shell example.

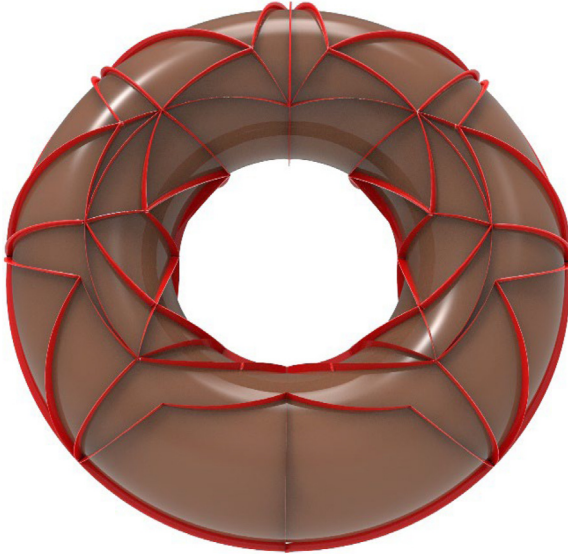


Fig. 25. The CAD model of the optimized structure (rib-reinforced torus-shaped shell example).

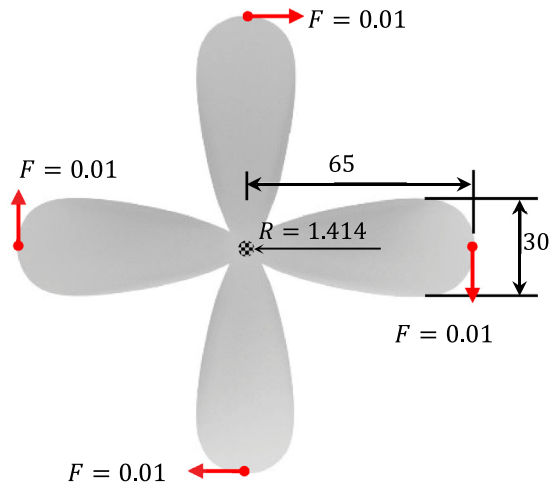
final optimized results are obviously very different. The reduction in the thickness of the base panel calls for more ribs to be placed on the base panel to enhance the stiffness of the thin-walled structures. Furthermore, there are some unconnected ribs generated in the optimized structure with a base panel thickness of $t_b = 3$, $t_b = 2$ and $t_b = 1$. Actually, similar phenomena of unconnected ribs were also observed in the work of other researchers. For example, in [31], the authors found that, under some circumstances, the structures with unconnected ribs perform better compared to the structures with connected ribs. However, since only the minimum compliance problem is considered in the present work, the performance of the unconnected ribs in more application scenarios is left for further investigation.

5.2. A rib-reinforced torus-shaped shell example

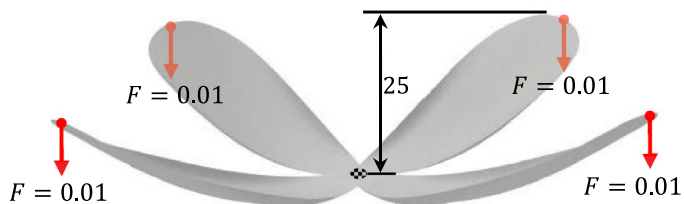
The second example investigates the reinforced-rib layout problem on the torus-shaped surface, which verifies the capability of the proposed method to deal with rib-reinforced thin-walled structures with non-zero genus surfaces. Some information about the problem setting is illustrated in Fig. 19. Eight concentrated loads with decreasing magnitudes are applied symmetrically along the surface's normal direction at each point, and the inner circle is restrained by the fixed end. The original torus-shaped surface mesh model contains 40 126 nodes and 80 252 elements totally with an average element size of 1.2. During the iteration process, the thickness of the base panel and the height of ribs are fixed as $t_b = 0.01$ and $h_r = 2$, respectively. The thickness of each rib (with initial value $t = 0.2$) is constrained to vary in the range of $[0.0001, 0.5]$, and the upper bound of the volume of the reinforced ribs is taken as $\bar{V} = 0.03 |D|$.

Since the genus of the torus surface is non-zero, there does not exist any homeomorphism between the current surface and the planar rectangular parameter domain. Hence, the surface cutting operation is introduced to generate an intermediate surface to assist in establishing the connection between the original torus surface and the planar parameter domain. As depicted in Fig. 20, the torus surface is firstly cut along two intersecting circles, and then a bijective mapping between the intermediate surface and the parameter domain is constructed utilizing the CCM technique. The initial design with 192 ribs and 308 design variables is displayed in Fig. 21, where component-based ribs are constructed in the parametric space first and then mapped back to the original surface characterizing the ribs layout in the physical space.

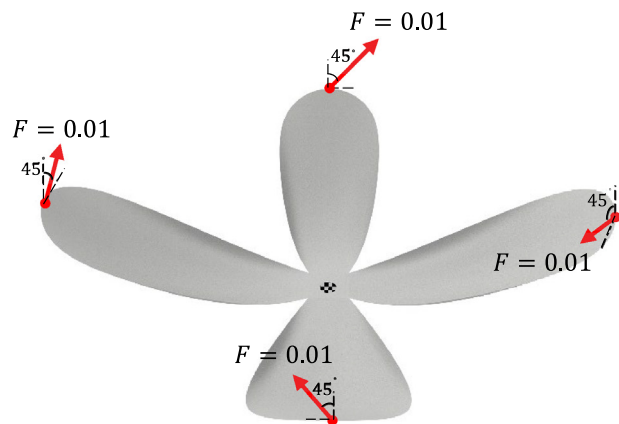
Layout optimization design can be carried out once the correspondence between the torus surface and a planar rectangle has been built. Fig. 22 illustrates some intermediate designs of the current example. Due to the magnitudes of concentrated loads decreasing from top to bottom, hence in the iteration process, it can be observed that material



(a) Case 1.



(b) Case 2.



(c) Case 3.

Fig. 26. The rib-reinforced flower-shaped shell example.

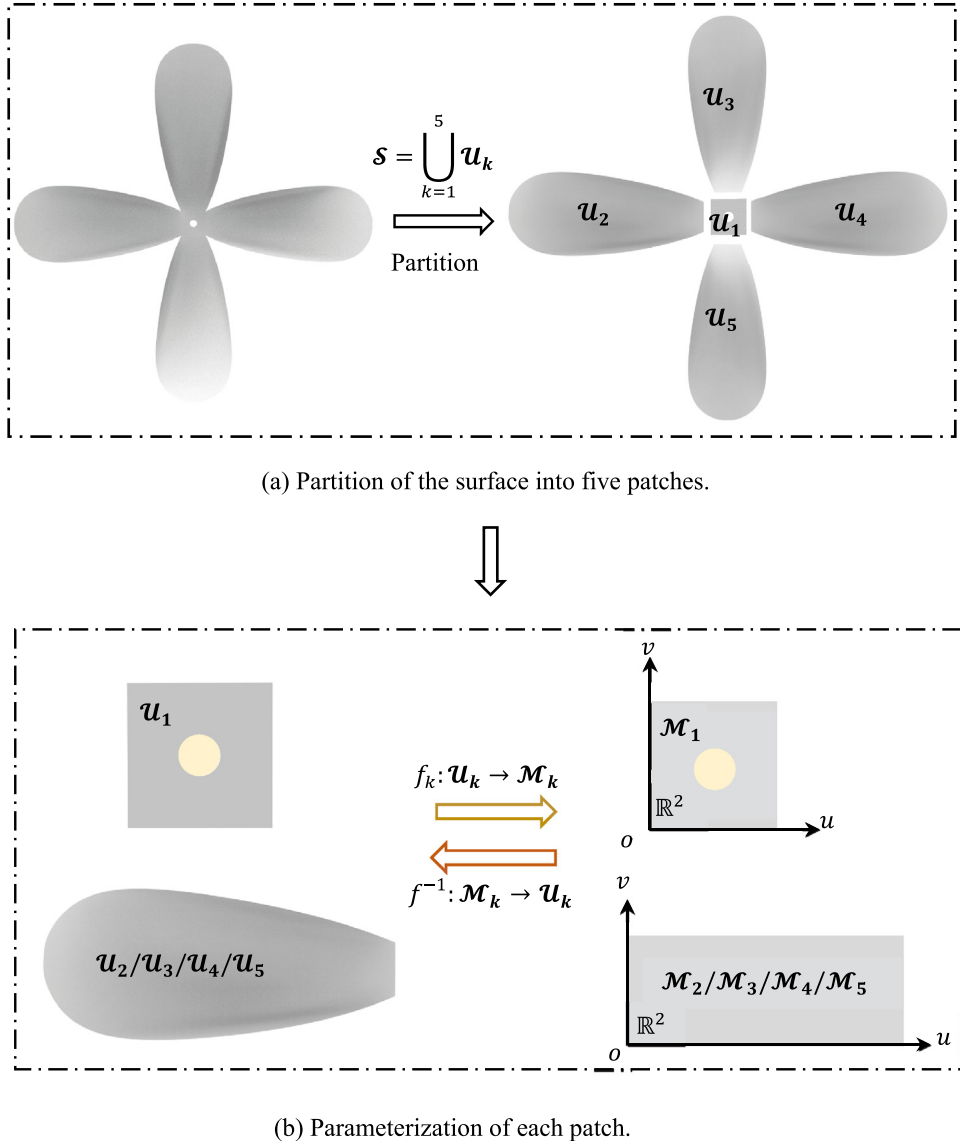
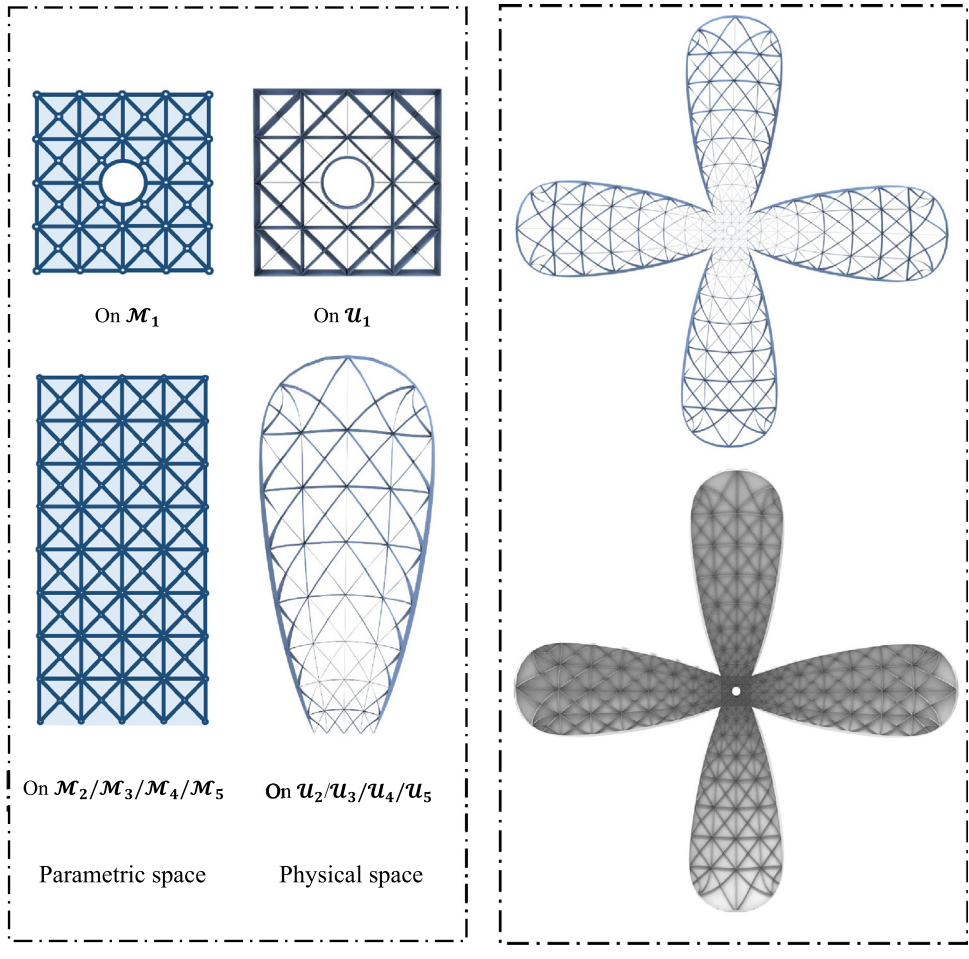


Fig. 27. Parameterization of the rib-reinforced flower-shaped shell example.

gathers gradually in the upper domain of the torus surface and related ribs are strengthened too. As the iteration continues, the thickness of ribs below the torus surface decreases and eventually stays stable. The iteration history of the objective and constraint function curves are provided in Fig. 23. The value of structural compliance decreases sharply in the first 15 steps and slows down gradually. At about the 250th step, the curves tend to be stable. The final optimized design with an objective function value of $C^{opt} = 131.59$ is exhibited in Fig. 24, where those ribs with thicknesses smaller than $t_r = 0.01$ have been removed in the optimized design. It can be observed that ribs with a clear layout seamlessly adhere to the surface of the base shell, and the CAD model of the optimized structure (see Fig. 25) can be easily exported without tedious post-processing.



(a) Initial rib layout on each patch.

(b) Assembling of all patches.

Fig. 28. The initial rib layout of the rib-reinforced flower-shaped shell example.

5.3. A rib-reinforced flower-shaped shell example

In this example, the rib layout optimization problem of a flower-shaped thin-walled structure is considered. The corresponding geometric model of this structure can be seen in Fig. 26. Noticing that although this structure has a simple topology, the shape of its geometry is somewhat complex. For such a structure, if the global conformal mapping is established by only one patch, the complexity of the surface shape will inevitably lead to excessive irregularity and distortion of the rib layouts in the physical space although the thin-walled components in the parameter space are evenly distributed via the ground structure technique. With this in mind, the multi-patch stitching scheme is adopted in this example and the surface of the structure is accordingly partitioned into five patches (see Fig. 27(a)). Then each flower patch can be directly mapped to a regular plane by the conformal mapping technique. For the middle patch, it is topologically equivalent to a square with an inner hole. Under this circumstance, not only the cutting operation but also a so-called hole-filling operation can be utilized to establish parameterization. In this example, we use the hole-filling operation. To be specific, the hole in the middle patch is first filled by Delaunay triangularization [58,59] and the filled patch is conformally mapped to a square. Then by deleting the triangular mesh associated with this hole in the square, the finally conformal mapping relationship between the middle patch

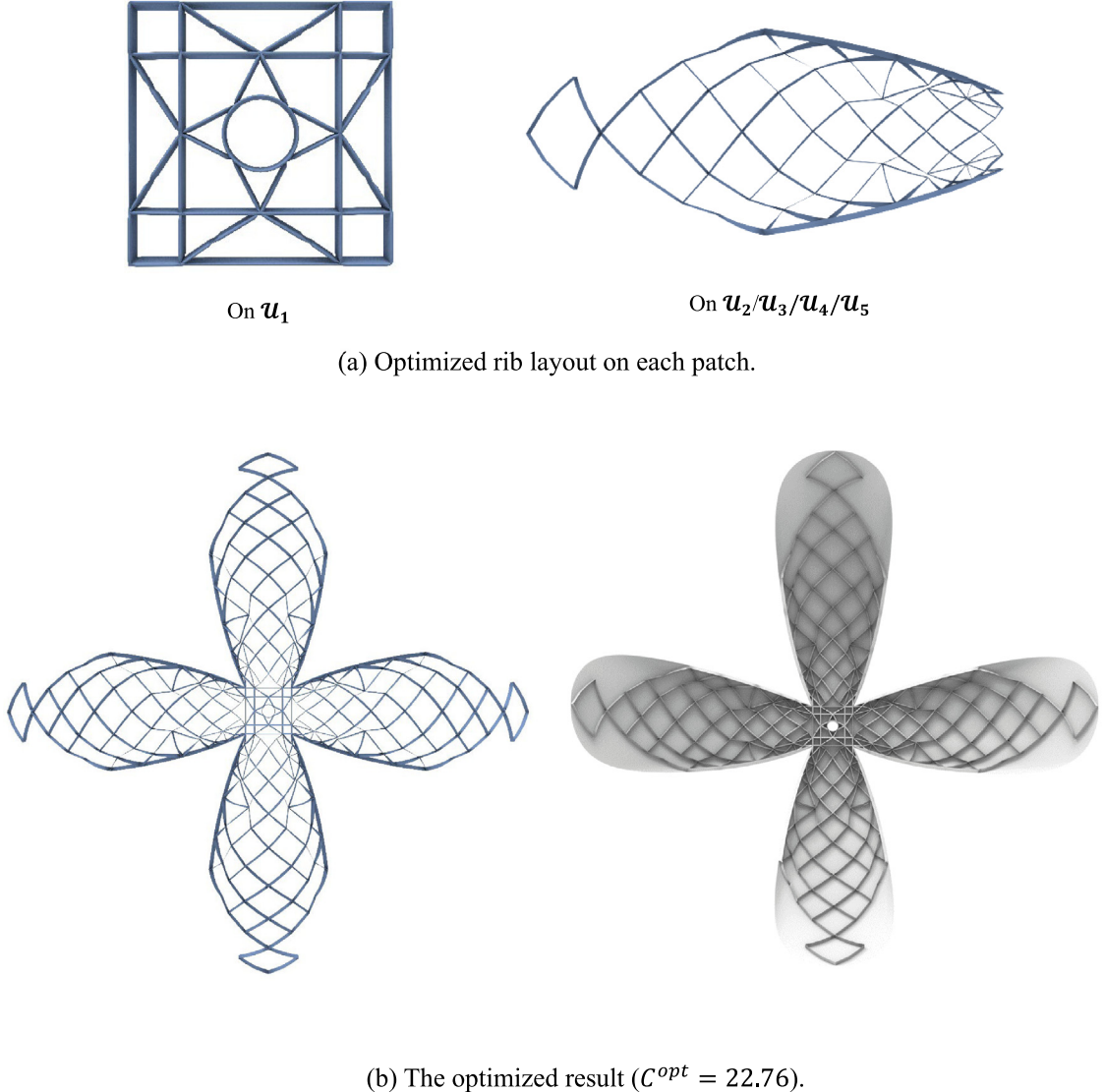
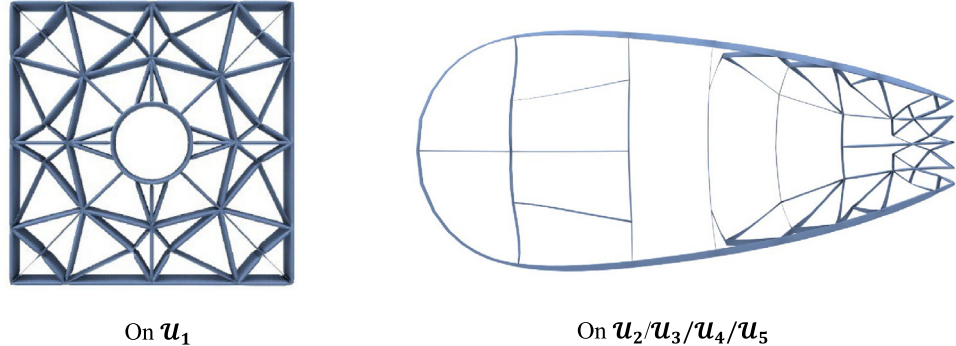


Fig. 29. The optimized design of the rib-reinforced flower-shaped shell example (case 1).

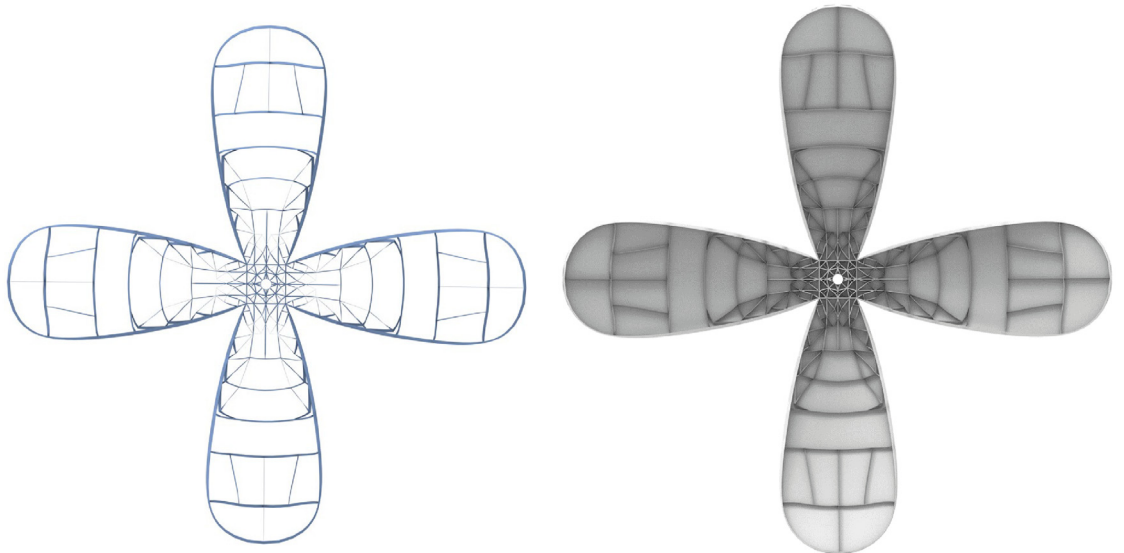
and the square with a hole is built (see Fig. 27(b)). Totally, the mesh model of the base surface consists of 98 664 triangular elements.

As shown in Fig. 26, for this example, we consider three different load cases for investigating the optimized designs under torsion, bending and bending-torsional coupling. The height of the ribs is set as $h_r = 1$ and the thickness of the base panel is set to $t_b = 0.01$. The upper bound of the rib's volume is set as $\bar{V} = 0.0375 |D|$. The initial design composed of 905 ribs and 1469 design variables is used in all three cases. Fig. 28. illustrates the initial rib layouts on each patch and the overall initial designs on the thin-walled structure. It should be pointed out that around the hole of the middle patch, an annular rib is also built to enhance the local stiffness, and the height of this rib is set to $h_a = 1.25$. The thickness of each rib (with initial value $t = 0.05$) is only allowed to vary in the range of $[0.0001, 0.25]$. All driven nodes are restricted to move within the design domain defined by the respective patches. The threshold for removing the narrow ribs is set as $t_r = 0.01$ in this example.

The optimized structures with the compliance values of 22.76, 96.23 and 71.95 for the three cases are provided in Fig. 29, Fig. 30 and Fig. 31, respectively. As can be observed, for all cases, optimized designs with clear rib



(a) Optimized rib layout on each patch.

(b) The optimized result ($C^{opt} = 96.23$).**Fig. 30.** The optimized design of the rib-reinforced flower-shaped shell example (case 2).

layouts and clean geometric features are generated. As can be seen from Fig. 29, under case 1, several cross-shaped ribs form the main force transmission paths to transfer the torque loads to the fixed end, which is quite reasonable from the mechanical point of view. In case 2, the obtained reinforced ribs are mainly distributed near the fixed end (see Fig. 30), which is quite different from the optimized designs under case 1. Such a design can obviously resist bending deformation very effectively. Compared with the optimized designs of Case 1 and Case 2, the optimized structure shown in Fig. 31 can be regarded as an ingenious combination of the results obtained under pure bending and pure torsion. The iteration histories of the three cases are provided in Fig. 32, and the stiffness improvements of the optimized designs reach 63.9%, 62.4% and 55.3%, respectively.

5.4. A rib-reinforced tee-branch pipe example

In the last example, the structure considered is a tee-branch pipe with a complex surface shape, as shown in Fig. 33. The interested readers can download the file of the corresponding geometry model from <https://github.com>

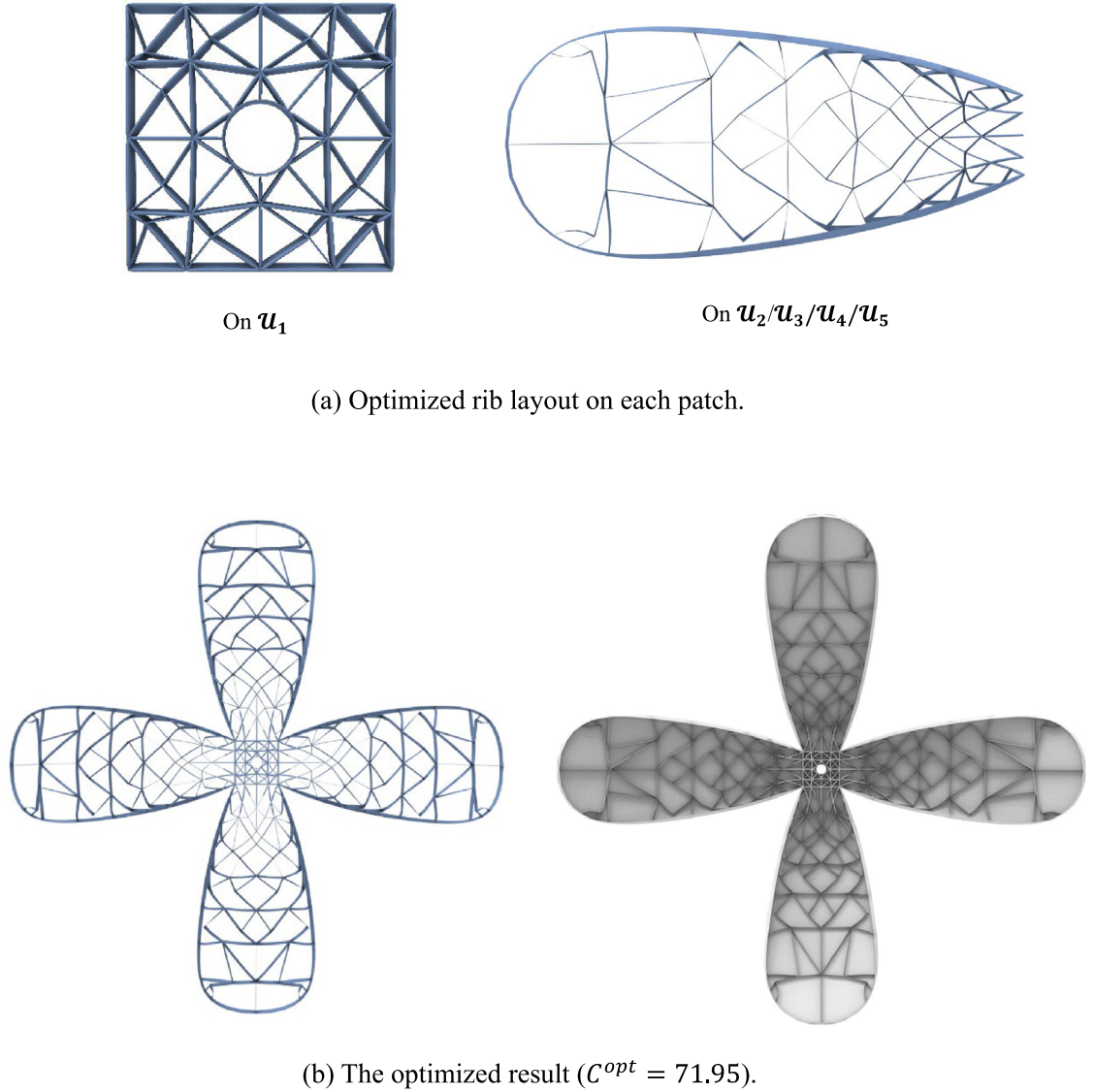


Fig. 31. The optimized design of the rib-reinforced flower-shaped shell example (case 3).

/Wendong-Huo/LibSurface/tree/main/inp_files or contact the authors for more details. The height of the ribs is set as $h_r = 0.001$ and the thickness of the base panel is set to $t_b = 0.0001$. The upper bound of the volume of the reinforced ribs is taken as $\bar{V} = 0.06 |D|$ and the thickness of each rib (with initial value of $t = 0.0001$) is set to vary in the range of $[10^{-7}, 0.0004]$. The total number of triangular elements used to simulate the base surface of this example is 107 784. Considering that the topology and shape of the structure are very complex, both the stitching operation and the cutting operation are required to establish the conformal mapping. As shown in Fig. 34(a), the entire surface is divided into four patches, where the three branch patches are connected to the joint patch. By trimming each branch patch along the direction of its generatrix, the relationship of conformal mapping between each branch patch and a rectangular domain can be directly established. For the joint patch, after cutting it along a selected line, it is topologically equivalent to a rectangle with an inner hole. Therefore, hole-filling operation

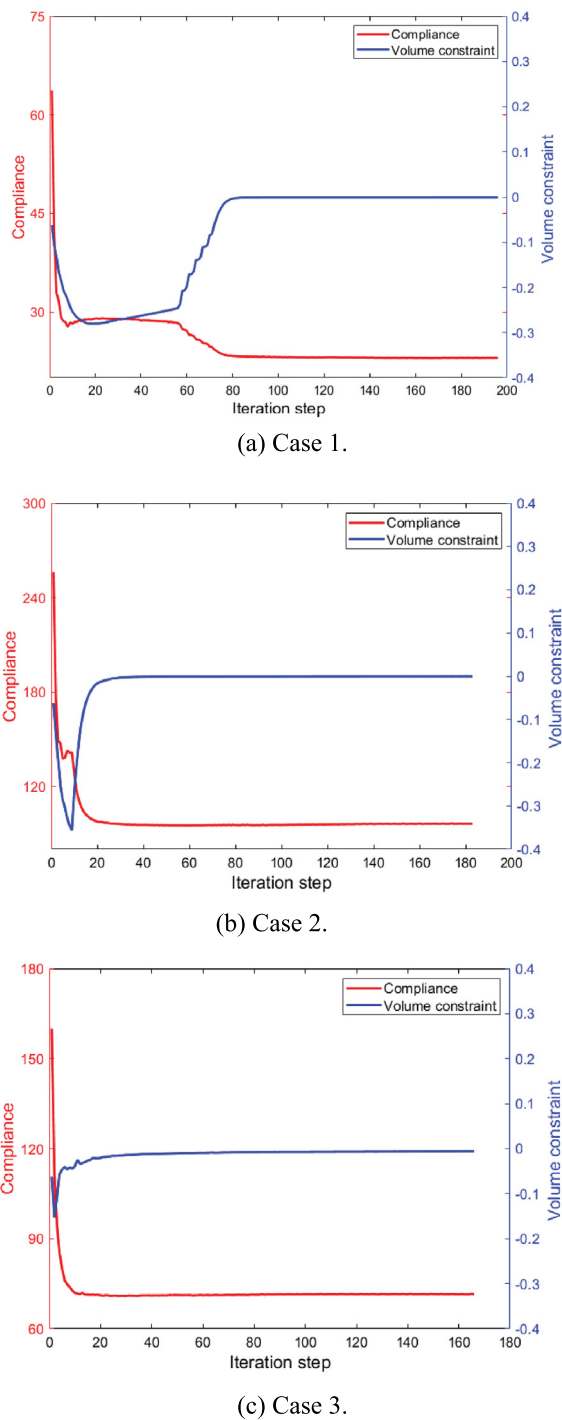
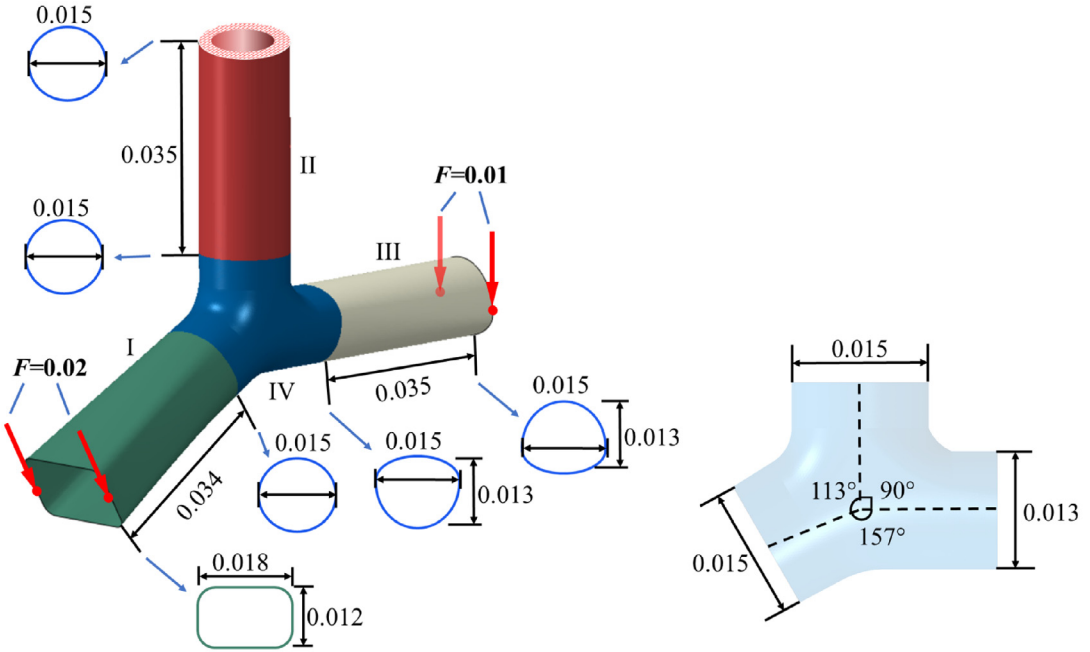


Fig. 32. The iteration history of the rib-reinforced flower-shaped shell example.



(a) Global view of the considered structure. (b) Geometry details of the surface IV.

Fig. 33. The rib-reinforced tee-branch pipe example.

used in the previous example can be used again to establish the conformal mapping of this patch (see Fig. 34(b)). Once finishing the construction of conformal mapping, the initial ribs can be built in the parametric space and the corresponding physical space. Fig. 35 shows the initial design with a total of 392 ribs, 163 driven nodes, and 638 design variables.

The optimized rib layout design and the corresponding iteration history for this example are presented in Fig. 36 and Fig. 37, respectively. The optimized value of the structural compliance is 559.24, which is reduced by about 33.1% compared to the initial design. Fig. 38(a) plots the distribution of the strain energy in the optimized structure. It can be seen from the figure that most thicker ribs are mainly distributed in the joint patch where the strain energy density is higher, which is in accord with the principle of minimum compliance design. Fig. 38(b) provides the stress distribution of the optimized design. It is worth noting that highly accurate analysis results about the reinforced ribs can be obtained by locally refining the mesh of the ribs via the adaptive meshing technique. Furthermore, since the obtained layout pattern is clear and clean and the boundaries of ribs are smooth enough, the optimized structure can also be imported into CAD/CAE systems with no additional post-processing (see Fig. 39) although the geometry and topology of the structure are complex.

6. Conclusions

This paper proposes an explicit layout optimization method for rib-reinforced thin-walled structures with complex geometries. This is achieved by first parameterizing the middle surface of a thin-walled structure through the Computational Conformal Mapping (CCM) technique, and then carrying out explicit layout optimization under the Moving Morphable Component (MMC)-based solution framework integrating with the surface cutting operation and the multi-patch stitching scheme on the parametric space.

The distinctive merits of this approach can be summarized as follows. Firstly, the intrinsic explicit geometry description provided by the MMC method ensures that a clear and clean rib layout with smoothly connected ribs can be obtained in the final optimized results. Accordingly, the optimized structural geometries can be easily imported into CAD/CAE systems without laborious post-process. Secondly, the construction, simulation and optimization

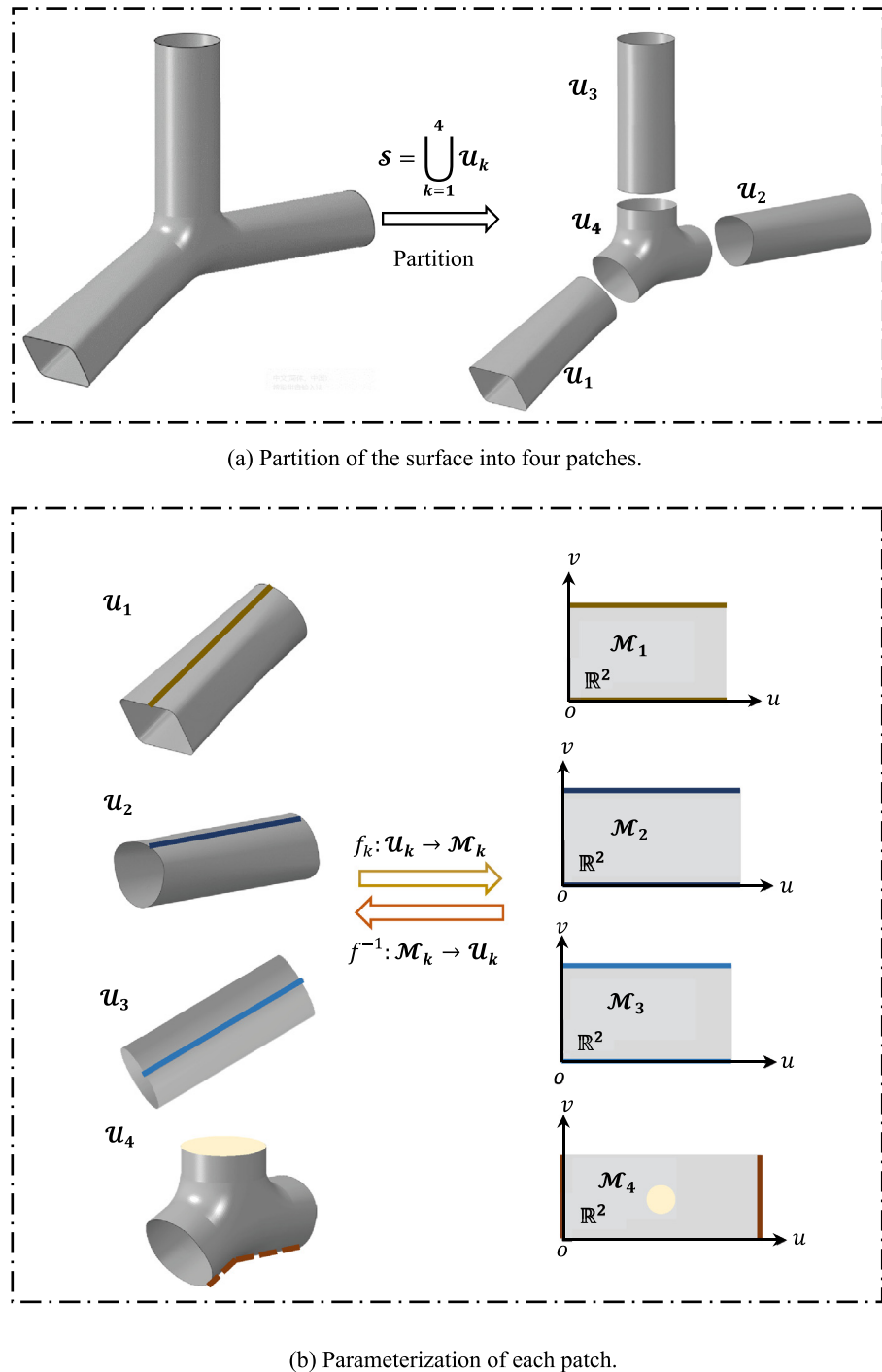


Fig. 34. Parameterization of the rib-reinforced tee-branch pipe example.

procedure of the rib-reinforced thin-walled structure are all accomplished based on a full-shell model discretized by adaptive body-fitted mesh, which can not only effectively relieve the computational burden, but also improve the accuracy of structural analysis. Last but not least, with the help of a computational conformal mapping technique

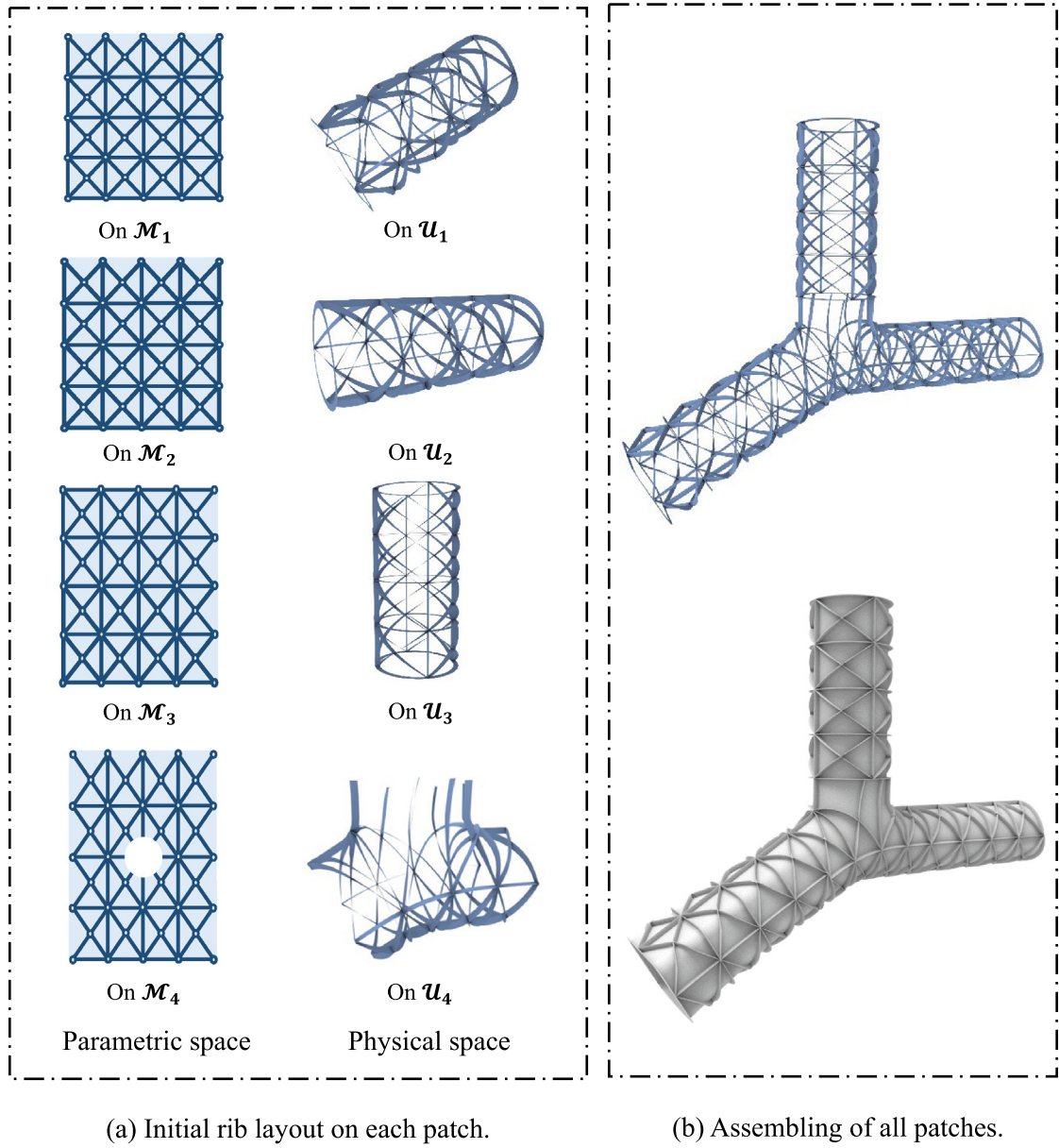
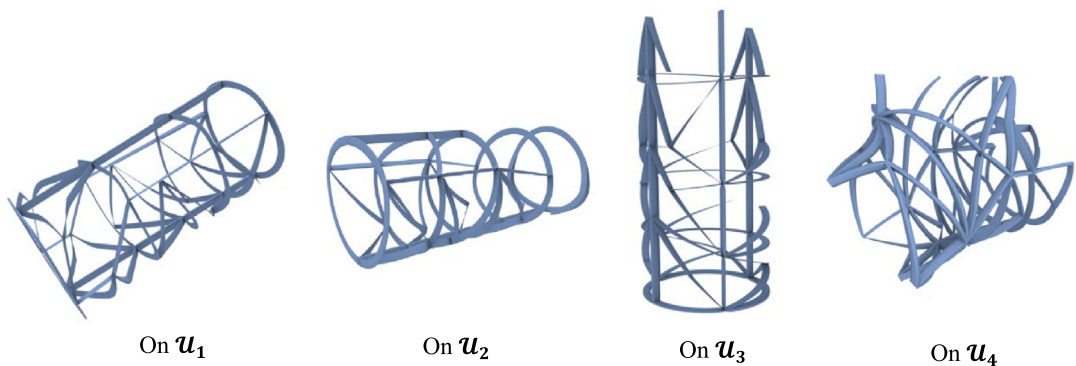


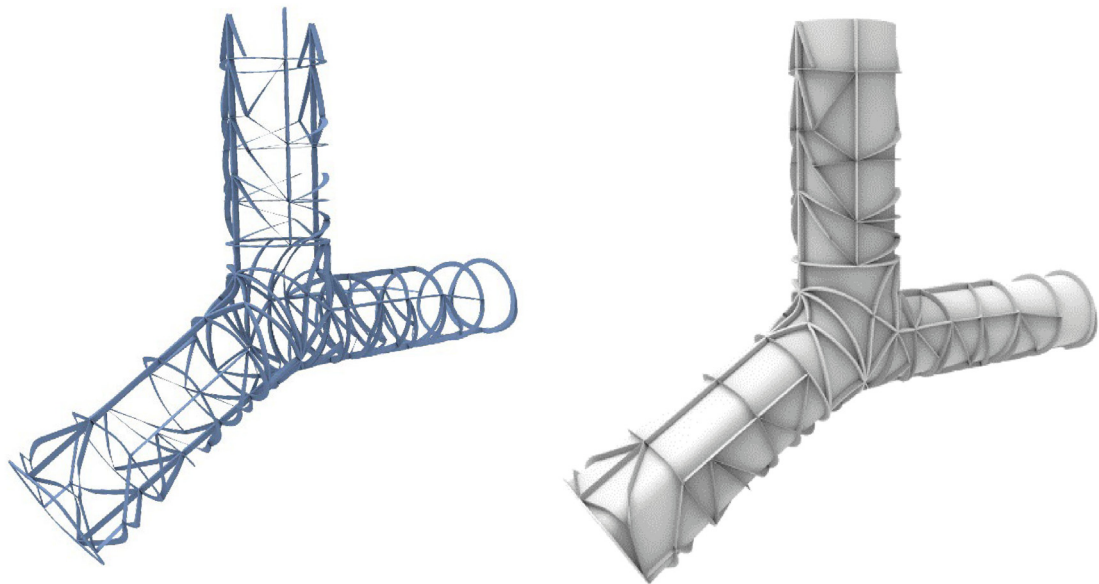
Fig. 35. The initial rib layout of the rib-reinforced tee-branch pipe example.

enhanced with the surface cutting and stitching operations, the proposed method can in principle address the rib layout optimization of thin-walled structures with arbitrary complex geometries.

It is worth noting that the present work is only a preliminary exploration of combining advanced computer graphics technology with explicit component-based optimization method where only structural compliance minimization is considered. Actually, one of the most important functionalities of rib-reinforcement construction is to prevent thin-walled structures from global/local buckling. Therefore, a natural extension of the present work is to incorporate buckling-related objective/constraint functions into the proposed solution framework. It is also very interesting to combine the present approach with machine learning techniques to achieve real-time design optimization of rib-reinforced thin-walled structures. Corresponding research results will be reported elsewhere.



(a) Optimized rib layout on each patch.

(b) The optimized result ($C^{opt} = 559.24$).**Fig. 36.** The optimized design of the rib-reinforced tee-branch pipe example.

Declaration of competing interest

The authors declare that they have no known competing financial interests or personal relationships that could have appeared to influence the work reported in this paper.

Data availability

No data was used for the research described in the article.

Acknowledgments

This work is supported by the National Key Research and Development Plan, PR China (2020YFB1709401), the National Natural Science Foundation, PR China (11821202, 11732004, 12002077, 12002073), the Fundamental

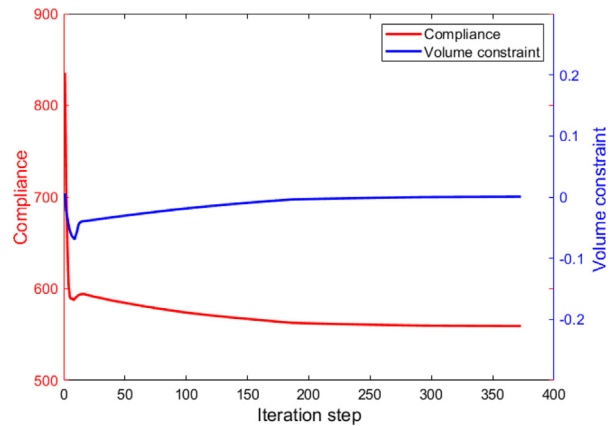
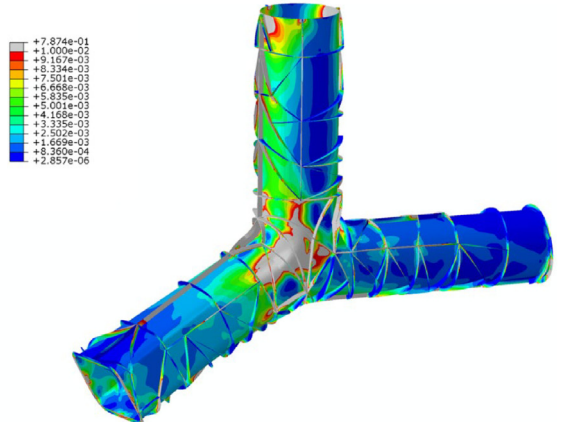
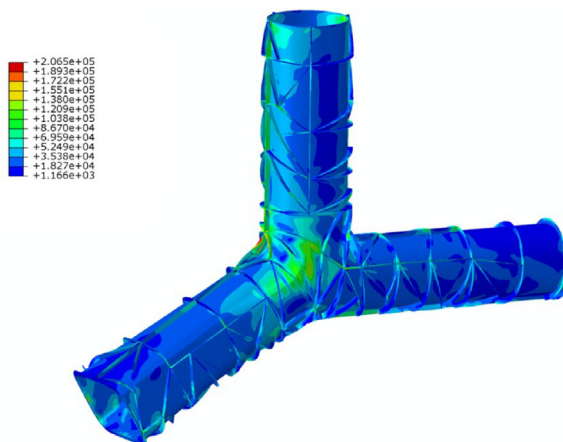


Fig. 37. The iteration history of the rib-reinforced tee-branch pipe example.



(a) Strain energy distribution.



(b) Stress distribution.

Fig. 38. The strain energy distribution and stress distribution in the optimized structure (rib-reinforced tee-branch pipe example).

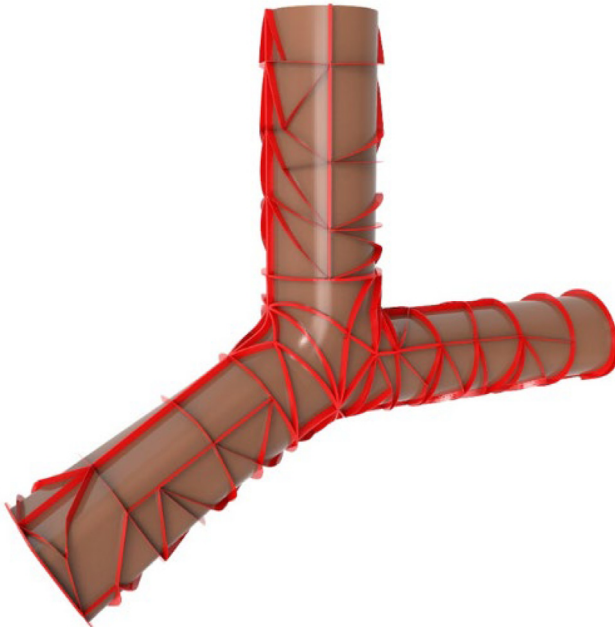


Fig. 39. The CAD model of the optimized structure (rib-reinforced tee-branch pipe example).

Research Funds for Central Universities, PR China (DUT21RC(3)076, DUT20RC(3)020), Doctoral Scientific Research Foundation of Liaoning Province, PR China (2021-BS-063) and 111 Project, PR China (B14013).

References

- [1] B.S. Jang, Y.S. Suh, E.K. Kim, T.H. Lee, Automatic FE modeler using stiffener-based mesh generation algorithm for ship structural analysis, *Mar. Struct.* 21 (2–3) (2008) 294–325.
- [2] P. Weizgraebel, C. Mittelstedt, W. Becker, Buckling of composite panels: A criterion for optimum stiffener design, *Aerospace Sci. Technol.* 16 (1) (2012) 10–18.
- [3] J. Loughlan, *Thin-Walled Structures: Advances in Research, Design and Manufacturing Technology*, CRC Press, 2018.
- [4] L. Wang, P.K. Basu, J.P. Leiva, Automobile body reinforcement by finite element optimization, *Finite Elem. Anal. Des.* 40 (8) (2004) 879–893.
- [5] K.T. Cheng, N. Olhoff, An investigation concerning optimal design of solid elastic plates, *Int. J. Solids Struct.* 17 (3) (1981) 305–323.
- [6] K.T. Cheng, N. Olhoff, Regularized formulation for optimal design of axisymmetric plates, *Int. J. Solids Struct.* 18 (2) (1982) 153–169.
- [7] R. Ansola, J. Canales, J.A. Tarrago, J. Rasmussen, Combined shape and reinforcement layout optimization of shell structures, *Struct. Multidiscip. Optim.* 27 (4) (2004) 219–227.
- [8] S.T. Liu, Q.H. Li, W.J. Chen, R. Hu, L.Y. Tong, H-DGTP—a Heaviside-function based directional growth topology parameterization for design optimization of stiffener layout and height of thin-walled structures, *Struct. Multidiscip. Optim.* 52 (5) (2015) 903–913.
- [9] A. Dugré, A. Vadean, J. Chausseé, Challenges of using topology optimization for the design of pressurized stiffened panels, *Struct. Multidiscip. Optim.* 53 (2) (2015) 303–320.
- [10] W. Saleem, A. Ahmed, A.A. Taimoor, Optimal design of ribbed-stiffened machined structures through material layout optimization, *J. Adv. Mech. Des. Syst.* 11 (2) (2017) JAMDSM0014.
- [11] N. Aage, E. Andreassen, B.S. Lazarov, O. Sigmund, Giga-voxel computational morphogenesis for structural design, *Nature* 550 (7674) (2017) 84–86.
- [12] N.D. Lagaros, M. Fragiadakis, M. Papadrakakis, Optimum design of shell structures with stiffening beams, *AIAA J.* 42 (1) (2004) 175–184.
- [13] P. Hao, B. Wang, G. Li, Z. Meng, K. Tian, X. Tang, Hybrid optimization of hierarchical stiffened shells based on smeared stiffener method and finite element method, *Thin-Walled Struct.* 82 (2014) 46–54.
- [14] P. Hao, B. Wang, K. Tian, G. Li, K. Du, F. Niu, Efficient optimization of cylindrical stiffened shells with reinforced cutouts by curvilinear stiffeners, *AIAA J.* 54 (4) (2016) 1350–1363.
- [15] B. Wang, K. Tian, P. Hao, Y. Zheng, Y. Ma, J. Wang, Numerical-based smeared stiffener method for global buckling analysis of grid-stiffened composite cylindrical shells, *Compos. Struct.* 152 (2016) 807–815.
- [16] D. Wang, M.M. Abdalla, Z.P. Wang, Z. Su, Streamline stiffener path optimization (SSPO) for embedded stiffener layout design of non-uniform curved grid-stiffened composite (NCGC) structures, *Comput. Methods Appl. Mech. Engrg.* 344 (2019) 1021–1050.

- [17] D. Wang, S.Y. Yeo, Z. Su, Z.P. Wang, M.M. Abdalla, Data-driven streamline stiffener path optimization (SSPO) for sparse stiffener layout design of non-uniform curved grid-stiffened composite (NCGC) structures, *Comput. Methods Appl. Mech. Engrg.* 365 (2020).
- [18] X.H. Ding, K. Yamazaki, Stiffener layout design for plate structures by growing and branching tree model (application to vibration-proof design), *Struct. Multidiscip. Optim.* 26 (1–2) (2004) 99–110.
- [19] Y. Ding, Z. Zhou, Z. Wang, H. Liu, K. Wang, Bionic stiffener layout optimization with a flexible plate in solar-powered UAV surface structure design, *Appl. Sci.* 9 (23) (2019).
- [20] X.H. Dong, X.H. Ding, G. Li, G.P. Lewis, Stiffener layout optimization of plate and shell structures for buckling problem by adaptive growth method, *Struct. Multidiscip. Optim.* (2019).
- [21] B.T. Li, C. Huang, C. Xuan, X. Liu, Dynamic stiffness design of plate/shell structures using explicit topology optimization, *Thin-Walled Struct.* 140 (2019) 542–564.
- [22] B.T. Li, H. Liu, Z. Yang, J. Zhang, Stiffness design of plate/shell structures by evolutionary topology optimization, *Thin-Walled Struct.* 141 (2019) 232–250.
- [23] B.T. Li, C. Xuan, W. Tang, Y. Zhu, K. Yan, Topology optimization of plate/shell structures with respect to eigenfrequencies using a biologically inspired algorithm, *Engrg. Optim.* 51 (11) (2018) 1829–1844.
- [24] L.Y. Li, C. Liu, W.S. Zhang, Z.L. Du, X. Guo, Combined model-based topology optimization of stiffened plate structures via MMC approach, *Int. J. Mech. Sci.* 208 (2021).
- [25] C. Bakker, L. Zhang, K. Higginson, F.v. Keulen, Simultaneous optimization of topology and layout of modular stiffeners on shells and plates, *Struct. Multidiscip. Optim.* 64 (5) (2021) 3147–3161.
- [26] S. Chu, S. Townsend, C. Featherston, H.A. Kim, Simultaneous layout and topology optimization of curved stiffened panels, *AIAA J.* 59 (7) (2021) 2768–2783.
- [27] S.Q. Feng, W.H. Zhang, L. Meng, Z. Xu, L. Chen, Stiffener layout optimization of shell structures with B-spline parameterization method, *Struct. Multidiscip. Optim.* 63 (2021) 2637–2651.
- [28] F. Savine, F.X. Irisarri, C. Julien, A. Vincenti, Y. Guerin, A component-based method for the optimization of stiffener layout on large cylindrical rib-stiffened shell structures, *Struct. Multidiscip. Optim.* (2021).
- [29] H. Liu, Z. Zhang, B. Li, M. Xie, J. Hong, S. Zheng, Topology optimization of high frequency vibration problems using the EFEM-based approach, *Thin-Walled Struct.* 160 (2021).
- [30] Q.H. Li, Y.X. Qu, Y.F. Luo, S.T. Liu, Concurrent topology optimization design of stiffener layout and cross-section for thin-walled structures, *Acta Mech. Sin.* 37 (3) (2021) 472–481.
- [31] E.A. Träff, O. Sigmund, N. Aage, Topology optimization of ultra high resolution shell structures, *Thin-Walled Struct.* 160 (2021).
- [32] Y. Deng, Z. Liu, J.G. Korvink, Topology optimization on two-dimensional manifolds, *Comput. Methods Appl. Mech. Engrg.* 364 (2020).
- [33] B. Hassani, S.M. Tavakkoli, H. Ghasemnejad, Simultaneous shape and topology optimization of shell structures, *Struct. Multidiscip. Optim.* 48 (1) (2013) 221–233.
- [34] W.S. Zhang, S. Jiang, C. Liu, D.D. Li, P. Kang, S.K. Youn, X. Guo, Stress-related topology optimization of shell structures using IGA/TSA-based moving morphable void (MMV) approach, *Comput. Methods Appl. Mech. Engrg.* 366 (2020).
- [35] T.J.R. Hughes, J.A. Cottrell, Y. Bazilevs, Isogeometric analysis: CAD, finite elements, NURBS, exact geometry and mesh refinement, *Comput. Methods Appl. Mech. Engrg.* 194 (39–41) (2005) 4135–4195.
- [36] W.H. Zhang, S.Q. Feng, Combined parameterization of material distribution and surface mesh for stiffener layout optimization of complex surfaces, *Struct. Multidiscip. Optim.* 65 (2022).
- [37] Q. Ye, Y. Guo, S. Chen, N. Lei, X.D. Gu, Topology optimization of conformal structures on manifolds using extended level set methods (X-LSM) and conformal geometry theory, *Comput. Methods Appl. Mech. Engrg.* 344 (2019) 164–185.
- [38] W.D. Huo, C. Liu, Z.L. Du, X.D. Jiang, Z.Y. Liu, X. Guo, Topology optimization on complex surfaces based on the moving morphable components (MMCs) method and computational conformal mapping (CCM), *Trans. ASME J. Appl. Mech.* 89 (2022).
- [39] X. Guo, W.S. Zhang, W.L. Zhong, Doing topology optimization explicitly and geometrically—A new moving morphable components based framework, *Trans. ASME J. Appl. Mech.* 81 (2014) 081009-1–081009-12.
- [40] W.S. Zhang, J. Zhang, X. Guo, Lagrangian description based topology optimization—A revival of shape optimization, *Trans. ASME J. Appl. Mech.* 83 (2016) 041010-1–041010-16.
- [41] G.P.T. Choi, H.L. Chan, R. Yong, S. Ranjitkar, A. Brook, G. Townsend, K. Chen, L.M. Lui, Tooth morphometry using quasi-conformal theory, *Pattern Recogn.* 99 (2020).
- [42] G.P.T. Choi, Y. Leung-Liu, X. Gu, L.M. Lui, Parallelizable global conformal parameterization of simply-connected surfaces via partial welding, *SIAM J. Imaging Sci.* 13 (3) (2020) 1049–1083.
- [43] Y. Guo, Q. Ye, X. Zheng, S. Chen, N. Lei, Y. Zhang, D.X. Gu, Computational generation and conformal fabrication of woven fabric structures by harmonic foliation, *Comput. Methods Appl. Mech. Engrg.* 363 (2020).
- [44] J. Tian, M. Li, Z. Han, Y. Chen, X.D. Gu, Q.J. Ge, S. Chen, Conformal topology optimization of multi-material ferromagnetic soft active structures using an extended level set method, *Comput. Methods Appl. Mech. Engrg.* 389 (2022).
- [45] L.M. Lui, K.C. Lam, T.W. Wong, X. Gu, Texture map and video compression using beltrami representation, *SIAM J. Imaging Sci.* 6 (4) (2013) 1880–1902.
- [46] T.W. Meng, G.P.T. Choi, L.M. Lui, TEMPO: Feature-endowed teichmüller extremal mappings of point clouds, *SIAM J. Imaging Sci.* 9 (4) (2016) 1922–1962.
- [47] U. Pinkall, K. Polthier, Computing discrete minimal surfaces and their conjugates, *Exp. Math.* 2 (1) (1993) 15–36.
- [48] X.D. Jiang, C. Liu, Z.L. Du, W.D. Huo, X.Y. Zhang, F. Liu, X. Guo, A unified framework for explicit layout/topology optimization of thin-walled structures based on moving morphable components (MMC) method and adaptive ground structure approach, *Comput. Methods Appl. Mech. Engrg.* 396 (2022).

- [49] S. Kargaran, B. Jüttler, S.K. Kleiss, A. Mantzaflaris, T. Takacs, Overlapping multi-patch structures in isogeometric analysis, *Comput. Methods Appl. Mech. Engrg.* 356 (2019) 325–353.
- [50] P.V. Sander, Z.J. Wood, S.J. Gortler, J.M. Snyder, H.H. Hoppe, Multi-chart geometry images, Google patents, 2007.
- [51] J. Xu, F. Chen, J. Deng, Two-dimensional domain decomposition based on skeleton computation for parameterization and isogeometric analysis, *Comput. Methods Appl. Mech. Engrg.* 284 (2015) 541–555.
- [52] D. Chapelle, K.-J. Bathe, *The Finite Element Analysis of Shells-Fundamentals*, Springer Science & Business Media, 2010.
- [53] Abaqus Analysis User's Manual, <https://www.abaqus.com>.
- [54] V. Komkov, K.K. Choi, E.J. Haug, *Design Sensitivity Analysis of Structural Systems*, Academic Press, 1986.
- [55] E. Laporte, P. Le Tallec, *Numerical Methods in Sensitivity Analysis and Shape Optimization*, Springer Science & Business Media, 2002.
- [56] K. Svanberg, The method of moving asymptotes—a new method for structural optimization, *Internat. J. Numer. Methods Engrg.* 24 (1987) 359–373.
- [57] M. Isenburg, P. Lindstrom, Streaming meshes, in: *Proceedings of the IEEE Visualization Conference*, 2005.
- [58] P.O. Persson, G. Strang, A simple mesh generator in MATLAB, *SIAM Rev.* 46 (2) (2004) 329–345.
- [59] J.R. Shewchuk, Triangle: Engineering a 2D quality mesh generator and delaunay triangulator, in: *Workshop on Applied Computational Geometry*, Springer, 1996, pp. 203–222.